Remote Sensing of Environment 307 (2024) 114150

Contents lists available at ScienceDirect

Remote Sensing of Environment

journal homepage: www.elsevier.com/locate/rse

Modeling gross primary production and transpiration from sun-induced chlorophyll fluorescence using a mechanistic light-response approach

Quentin Beauclaire [a,*], Simon De Cannière [b], François Jonard [c,b], Natacha Pezzetti [a], Laura Delhez [a], Bernard Longdoz [a]

[a] BIODYNE Biosystems Dynamics and Exchanges, TERRA Teaching and Research Center, Gembloux Agro-Bio Tech, University of Liege, Liege, Belgium
[b] Agrosphere (IBG-3), Institute of Bio- and Geosciences, Jülich Research Centre, Jülich, Germany
[c] Earth Observation and Ecosystem Modeling Laboratory, SPHERES Research Unit, University of Liege, Liege, Belgium

ARTICLE INFO

Edited by Jing M. Chen

Keywords:
GPP
SIF
Transpiration
MLR
Modeling
Wheat

ABSTRACT

Sun-induced chlorophyll fluorescence (SIF) is a promising optical remote sensing signal which is directly linked to photosynthesis, allowing for the monitoring of gross primary production (GPP). Although empirical relationships between these variables have demonstrated the potential of SIF for site-specific GPP estimations, a better physiological understanding of the link between SIF and GPP would pave the way for a more robust model of photosynthesis. The mechanistic light response (MLR) model is a novel approach which determines GPP from SIF by using only a small set of equations and parameters with physiological significance. This study combines the MLR model with the unified stomatal optimality (USO) model to estimate both GPP and transpiration (Tr) at the ecosystem scale. Top-of-canopy SIF measurements were collected over a winter crop with a field spectrometer installed next to an eddy covariance station. MLR-USO model parameters were determined from gas exchange and active chlorophyll fluorescence measurements at the leaf level and interpolated on a half-hourly basis using solar irradiance and canopy temperature. GPP and Tr estimated by the MLR-USO model and eddy covariance measurements were highly correlated at half-hourly and daily timescales ($R^2 \geq 0.91$, rRMSE $\leq$ 13.7%) under a wide range of environmental conditions, including soil water stress. These results highlight the potential of the MLR-USO model as an important step towards an improvement of our understanding of the coupling between the water and carbon cycles at the ecosystem scale and beyond.

1. Introduction

Each year, terrestrial ecosystems uptake approximately one-third of the carbon emitted by human activities (Friedlingstein et al., 2022). Gross primary production (GPP) of terrestrial ecosystems represents the most important flux in the global carbon cycle (Beer et al., 2010) and plays a central role in regulating atmospheric CO_2 concentration (Sha et al., 2022).

Anthropogenic climate change increases the occurrence of climate extremes such as droughts or heatwaves, which causes a reduction in GPP (Williams et al., 2014; Reichstein et al., 2013). Whether terrestrial ecosystems will keep removing as much CO_2 from the atmosphere or become CO_2 sources is highly uncertain as most land surface models (LSMs) predict various future ecosystem uptake abilities in a climate change context (Ryu et al., 2019). Quantifying and modeling GPP at global scales is therefore crucial to better understand how climate extremes constrain primary production in climate modeling.

GPP is the total amount of carbon fixed by ecosystems and originates from complex photosynthetic processes that cannot be directly measured. The standard approach for estimating GPP at the ecosystem scale is the measurement of the net ecosystem exchange (NEE) with the eddy covariance (EC) technique, and its partitioning between ecosystem respiration (R_{ECO}) and GPP. More than 200 EC sites are currently part of the FLUXNET network, which regroups over 1500 site-years of data (Baldocchi, 2014; Pastorello et al., 2020). However, flux towers are unevenly distributed across the globe, which explains that the temporal and spatial representativeness of flux measurements (the extrapolation of flux information to extended spatial and timescales) has become an increasingly important issue for the scientific community to provide flux information "everywhere and all the time" (Chu et al., 2017; Chu et al.,

* Corresponding author.
E-mail addresses: q.beauclaire@uliege.be (Q. Beauclaire), s.de.canniere@fz-juelich.de (S. De Cannière), Francois.Jonard@uliege.be (F. Jonard), laura.delhez@uliege.be (L. Delhez), Bernard.Longdoz@uliege.be (B. Longdoz).

https://doi.org/10.1016/j.rse.2024.114150
Received 17 October 2023; Received in revised form 22 March 2024; Accepted 5 April 2024

2021). In addition, the size and shape of flux tower footprints (the source areas of EC fluxes) are directly affected by meteorological variables (such as wind direction or air turbulence) and surface roughness, which complicates the interpretation of GPP from local to global scales (Kong et al., 2022). Most of the recent approaches for upscaling carbon assimilation to large scales use machine learning to build empirical models between remote sensing (RS) data and ground observations of GPP (Jung et al., 2020).

Photosynthesis is a complex chain of photochemical and enzymatical reactions, which are commonly categorized between the light reactions (which generate ATP and NADPH from light and water) and the dark reactions (which transform CO_2 into carbohydrates using ATP and NADPH). Sun-induced chlorophyll fluorescence (SIF) originates from the emission of photons in the red and far-red regions after the absorption of a fraction of photosynthetic active radiation (PAR) by chlorophyll *a* pigments during the light reactions of photosynthesis. Although SIF quantum yield is very low (~1 to 2%; Maxwell and Johnson, 2000) compared to photochemical quantum yield (PQ) and thermal energy dissipation (i.e., non-photochemical quantum yield NPQ), it is tightly coupled to GPP as these three processes are in competition for PAR. In particular, SIF is linked to the electron transport rate which fuels ATP and NADPH to the fixation sites in the chloroplasts (Gu et al., 2019). While the relationship between SIF and PQ quantum yields at the leaf level is highly nonlinear on short timescales (Porcar-Castell et al., 2014), large temporal and spatial scales data show a strong linearity between SIF and carbon assimilation (Lee et al., 2015; Damm et al., 2010; Li et al., 2018; Chen et al., 2019). Such relationship has been the basis of the calibration of empirical models between ground-based GPP and remotely sensed SIF for estimating GPP at global scale using the light use efficiency (LUE) approach (Porcar-Castell et al., 2014; Jonard et al., 2020; Li et al., 2018; Xiao et al., 2019). However, this concept does not allow to identify the actual mechanistic link between SIF and GPP, and there is a lack of knowledge about the influence of physiological and environmental factors on these relationships. A decoupling between SIF and GPP can be observed during stress episodes such as heatwaves (Wohlfahrt et al., 2018; Martini et al., 2022), drought (Helm et al., 2020; Marrs et al., 2020; Chen et al., 2020), light-limiting conditions (Chen et al., 2019), or for heterogeneous canopies (van der Tol et al., 2009; Gu et al., 2019). These examples illustrate the limits of using this approach across spatial scales and climate conditions.

A model must consider two aspects to estimate GPP from SIF with a mechanistic approach. First, the relationship between fluorescence and photochemistry must be characterized at the photosystem level. Second, the scattering and absorption effects of overlying leaves should be considered when the fluorescence photons travel through the canopy (Yang et al., 2019). The soil canopy observation photosynthesis energy (SCOPE; van der Tol et al., 2009) model integrates both the physiological and the canopy structural aspects of the SIF emission in separate sub-models. These aspects are highly dynamic and change in function of the plant water status (De Cannière et al., 2022; Wang et al., 2022). Although the SCOPE model is often used in a reduced form when coupled to other models, it is computationally intensive and requires numerous parameters, forcing the user to make a series of assumptions (e.g., Lee et al., 2015; De Cannière et al., 2021).

An alternative approach to link SIF and GPP is the mechanistic light response model (MLR; Gu et al., 2019). While the SCOPE model uses sub-models to integrate the physiological and structural aspects of SIF emission, the MLR model only considers few parameters which describe the energy partitioning at the PSII level (e.g., the fraction of open PSII center q_L and the maximum photochemical quantum yield $\phi_{PSII,max}$) and leaf-to-canopy radiative transfer processes (i.e., the escape probability factor f_{esc}) to determine the actual electron transport rate between the two photosystems (PSII and PSI). This mechanistic representation of the light reactions contrasts with the Farquhar-von Caemmerer-Berry (FvCB) model of photosynthesis (Farquhar et al., 1980) where the potential electron transport rate is determined from PAR by an empirical relationship. The FvCB model requires numerous parameters that are highly variable across plant functional types (PFT) and environmental conditions. Such uncertainties cause important disagreements in LSMs which use the FvCB model to estimate carbon assimilation (Rogers et al., 2017; Walker et al., 2021). By taking advantage of the physiological information carried by SIF, MLR model equations mechanistically describe photosynthetic processes while reducing the impact of parameter uncertainty (Han et al., 2022a, 2022b; Gu et al., 2019). With this approach, GPP can be estimated from electron requirements for carboxylation and oxygenation regardless of carboxylation limiting stages (Gu et al., 2019).

Stomatal opening controls both water and carbon exchanges at the leaf surface. Through stomatal regulation, plants balance water loss and carbon uptake (Cowan and Farquhar, 1977), leading to a close coupling between GPP and transpiration (Tr). Recent models simulating stomatal behavior such as the unified stomatal optimality model (USO; Medlyn et al., 2011) are based on the optimization of the ratio between benefit (i.e., carbon gain) and cost (i.e., water loss) of stomatal opening and on environmental variables such as vapor pressure deficit (VPD), GPP and CO_2 concentration at the leaf surface. Coupling the MLR and USO models (MLR-USO) provides a new, process-based approach for the modeling of carbon and water fluxes from SIF.

SIF can be retrieved by high-resolution measurements of vegetation spectral proprieties from sensors on masts, aircrafts or satellites (Mohammed et al., 2019; Jonard et al., 2020). For instance, spaceborne spectrometers such as the TROPOspheric Monitoring Instrument (TROPOMI) or the NASA's Orbiting Carbon Observatory (OCO-2, OCO-3) measure SIF emission at a specific wavelength (e.g., 740 nm for TROPOMI) from kilometer-scale footprints. These data have been used for training machine learning algorithms linking SIF and GPP with empirical linear regressions (Jung et al., 2020) or for investigating water and light limiting conditions on photosynthesis at large scales (Jonard et al., 2022). The upcoming FLuorescence EXplorer (FLEX) tandem mission with Sentinel-3 will enable the quantification of unique products related to SIF and surface temperature at a high spatial resolution (300 × 300 m; Drusch et al., 2017). Such improvement will reduce the current mismatch between flux tower footprint and RS products. Moreover, many studies have been designed to validate future FLEX products by measuring SIF with top-of-canopy (TOC) sensors such as the Fluorescence boX (FloX; JB Hyperspectral, Düsseldorf, Germany), whose development has been supported by the European Space Agency (ESA - Schuttemeyer et al., 2018). The MLR-USO model must be first evaluated at the ecosystem scale using TOC SIF measurements before future applications with remotely sensed SIF data at larger scales.

The MLR-USO model relies on a straightforward methodology for improving our understanding of the photosynthetic and transpiration processes by exploiting the physiological message carried by the SIF signal. To date, no studies have tested such a model. In this perspective, we used the MLR-USO model to estimate GPP and Tr from TOC SIF. This study focused on wheat, which is the most widely planted crop (Erenstein et al., 2022) and an important crop functional type in climate models (Lu et al., 2017; Boas et al., 2021). Our approach aimed at: (1) characterizing the relationship between SIF and GPP at the ecosystem scale for winter wheat, (2) measuring MLR-USO model parameters and assessing their dependence on meteorological variables and (3) validating MLR-USO model outputs with EC data.

2. Material and methods

2.1. Study site

All the measurements presented in this study were performed at the Integrated Carbon Observatory System (ICOS) station of Lonzée (BE-Lon, Level 2 ICOS station), located in the Wallonia region in Central Belgium (50°33′ N, 4°44′ E, 167 m asl). The Lonzée experimental site has been cultivated for more than 80 years based on a typical 4-year

rotation: winter wheat / sugar beet (*Beta vulgaris*) / winter wheat (*Tritcum aestivum*) / seed potato (*Solanum tuberosum*). The climate is temperate oceanic, with mean annual air temperature and cumulative precipitation of about 10.2 °C and 743 mm respectively. The soil is silty clay, with two main horizons: a ploughed layer from 0 to 35 cm (FAO classification Ap) and a layer enriched in clays (FAO classification Bt) from 35 to 100 cm depth (Table S1). This study exclusively focused on the 2022 growing season dedicated to winter wheat (*Triticum aestivum* cv. Skyscraper), which was sown on October 28, 2021 and harvested on July 24, 2022. No irrigation was applied during the growing season. Farming activities are summarized in Table S2.

2.2. Eddy covariance fluxes and meteorological measurements

The contribution of the target cropland to the EC fluxes was large regardless of the atmospheric conditions (>90% on average during the last 13 years, data not shown). The prevailing winds are SW and NE with a cropland fetch of respectively 240 m and 200 m. The sonic anemometer (Solent Research R3, Gill Instruments Lymington, UK) and gas analyzer (LI-7200, LI-COR, Lincoln, NE, US) of the EC station were selected following ICOS guidelines (Rebmann et al., 2018). Half-hourly fluxes of net CO_2 and latent heat (LE, from which Tr is thereafter determined) were computed from high frequency measurements (20 Hz) of vertical wind speed, CO_2 and H_2O concentrations at 2.93 m above the ground. These raw data were processed by the ICOS Ecosystem Thematic Center (ETC) using the ONEFlux pipeline (Pastorello et al., 2020) and are available in the ICOS Carbon Portal (Dumont et al., 2023). R_{ECO} and GPP were determined from NEE by using the nighttime partitioning method (Reichstein et al., 2005). Storage CO_2 fluxes were neglected owing to the short measurement height. Flux data corresponding to low turbulence conditions (with low friction velocity (u_*) were discarded from the analysis using the variable u_* threshold method (VUT; Pastorello et al., 2020), which is preferred when canopy cover changes throughout the years such as crops. Moreover, no gap-filled fluxes were selected (i.e., quality flag of 0). The variables GPP_NT_VUT_REF for GPP and LE_F_MDS for LE were selected from the dataset. These fluxes are referred to in this paper as GPP_{EC} and LE_{EC}.

Micrometeorological measurements were collected on a half-hourly basis, including incoming photosynthetic photon flux density in the photosynthetic active radiation (photodiode-based sensor - PAR Quantum sensor SKP 215, Skye Instruments Limited, Llandrindod Wells, UK), precipitation (weighing rain gauge - TRwS415, MPS system sro, Bratislava, SK), air temperature and relative humidity (resistive platinum thermometer and electrical capacitive hygrometer - HMP155, Vaisala Oyj, Helsinki, FI), soil heat flux (self-calibrating soil heat flux plate-HFP01SC, Hukseflux Thermal Sensors B.V., Delft, NL), longwave downward and outgoing fluxes, net radiation (pyradiometer – CNR 4, Kipp and Zonen, Delft, NL) and soil water content (SWC) at three different locations and at five different depths (5, 15, 25, 55 and 85 cm) using silicon bandgap temperature and capacitance sensors (EnviroSCAN Probe, Sentek Sensor Technologies, Stepney, SA, AU).

2.3. Spectral measurements of SIF

Solar irradiance and reflected radiance from the canopy were measured by the Fluorescence boX (FloX - JB Hyperspectral, Düsseldorf, Germany), which consists of two spectrometers: a QE Pro and a FLAME-S spectrometer (Ocean Optics, Inc., USA). QE Pro measures downwelling irradiance and upwelling radiance covering the range between 650 and 800 nm to observe the SIF signal in the O_2-A (760 nm) and O_2-B (687 nm) absorption bands while FLAME-S covers a wider range from 400 to 1000 nm including both visible and near-infrared (NIR) wavelengths. The QE Pro and FLAME-S spectrometers have a spectral sampling interval and spectral resolution of respectively 0.17 nm, 0.3 nm and 0.65 nm, 1.5 nm. The spectrometers are housed in a thermally regulated box which keeps temperature below 25 °C to avoid spectral shifts and dark current drifts. The optical fibers were installed on a mast at 2 m height, at approximately 20 m from the center of the plot, and 5 m from the location where one of the three soil water content sensor profiles was installed. The downward looking bare fibers have an opening angle of 23° which allows to measure the canopy reflectance and SIF emission over a footprint of approximately 1.5 m^2. The receptor of the upward looking fiber measuring the downwelling irradiance has a hemispherical field of view of 180°. The FloX was installed on February 24, 2022 and removed on July 18, 2022, few days before the harvest of winter wheat.

SIF was retrieved using the spectral fitting method (SFM) from the canopy reflectance spectrum in the O_2-A band which provides the most reliable SIF measurements (Cendrero-Mateo et al., 2019; Chang et al., 2020). The O_2-A band was preferred over the O_2-B band as it enables to track photosynthesis dynamics and limits the reabsorption effects within the canopy structure (Cendrero-Mateo et al., 2019; Martini et al., 2022). Moreover, dense cloud cover may complicate the retrieval of SIF. Therefore, days with a clearness index (i.e., the ratio between net radiation at the top of the canopy and extraterrestrial net radiation, Chang et al., 2020) lower than 0.3 were discarded from the analysis (Chen et al., 2020; Yang et al., 2021), as well as data measured when solar radiation is too low (before 9 am and after 3 pm; UTC + 1). Nonlinearity and spectral shift corrections on raw FloX measurements were applied. A threshold of solar zenithal angle of 70° was set to avoid detector saturation (Chang et al., 2021). TOC SIF retrieved with the SFM method within the O_2-A band is further referred to as $SIF_{TOC,760}$.

2.4. Downscaling of SIF from TOC to photosystem level

As SIF is affected by re-absorption and scattering effects of the canopy, $SIF_{TOC,760}$ is indirectly related to the SIF emitted by leaves. Estimating GPP with the MLR model requires the determination of the SIF signal emitted only from PSII at the leaf level over the broadband spectrum emission of fluorescence (Gu et al., 2019). Therefore, $SIF_{TOC,760}$ must be multiplied by three conversion factors representing (i) the fraction of PSII fluorescence emission contributing to the total SIF emission of the leaf (f_{PSII}), (ii) the integration of the SIF signal at 760 nm over the broadband spectrum emission of fluorescence (f_λ), and (iii) the effects of absorption and re-scattering by the canopy structure (f_{esc}^{-1}). Total SIF (SIF_{TOT}) was therefore calculated from $SIF_{TOC,760}$ by (Liu et al., 2022b):

$$SIF_{TOT} = \frac{SIF_{TOC,760} \cdot f_{PSII} \cdot f_\lambda}{f_{esc}} \quad (1)$$

The calculation steps of the three factors are detailed below.

2.4.1. Separating the contribution of PSII to SIF measurement

Both PSI and PSII contribute to the emission of SIF in the NIR. Therefore, the influence of PSI on $SIF_{TOC,760}$ must be considered before applying the MLR model which is valid only for PSII SIF emission. f_{PSII} was calculated as the ratio of chlorophyll fluorescence quantum yields at the leaf level, while accounting for the contribution of PSI (Jia et al., 2023). The detailed procedure of leaf-level measurements is given in section 2.9.

2.4.2. From top-of-canopy to leaf surface

f_{esc} is the escape probability that SIF photons emitted by PSII reach the top of the canopy. f_{esc} was determined as the ratio of NIR light originating from vegetation (NIR_v) to the fraction of incident PAR absorbed by the canopy (f_{APAR}) under the assumption of high leaf area index and low contribution of soil reflectance (Zeng et al., 2019):

$$f_{esc} = \frac{NIR_v}{f_{APAR}} \quad (2)$$

NIR_v was calculated from the normalized difference vegetation index (NDVI) and the canopy reflectance in the NIR (R_{NIR}; Badgley et al.,

2017):

$$NIR_v = (NDVI - NDVI_0)\cdot R_{NIR} = \left(\frac{R_{NIR} - R_{RED}}{R_{NIR} + R_{RED}} - NDVI_0\right)\cdot R_{NIR} \quad (3)$$

Where R_{RED} is the canopy reflectance in the red and $NDVI_0$ is the minimum NDVI and accounts for the effects of bare soil on NIR_v (Badgley et al., 2017). R_{NIR} and R_{RED} were measured by the FloX at respectively 760 nm and 680 nm. f_{APAR} was determined from $NDVI$ by using a linear model which has already been used to estimate wheat crop yields (Moriondo et al., 2007; Myneni and Williams, 1994):

$$f_{APAR} = 1.16\cdot NDVI - 0.14 \quad (4)$$

$NDVI_0$ was set to 0.12, which is the $NDVI$ value when f_{APAR} (Eq. 4) equals 0 (Myneni and Williams, 1994).

2.4.3. Integration of the SIF signal over the broadband fluorescence emission spectrum

The final step of the conversion of $SIF_{TOC,760}$ into SIF_{TOT} consists in integrating the SIF signal emitted by PSII at 760 nm over the broadband chlorophyll fluorescence emission spectrum, which requires broadband theoretical fluorescence emission spectrum of PSII. The SCOPE model (version 1.73; van der Tol et al., 2009) was used to simulate a total of 6720 chlorophyll fluorescence spectra between 650 and 840 nm from a canopy with different leaf biochemical and structural proprieties, sun-canopy sensor geometry and structure. The fluorescence spectrum that provided the most meaningful representation of the dataset was retrieved by the singular vector decomposition (SVD) technique (Liu et al., 2022b; Zhao et al., 2014). The first principal component explained more than 99% of the variance of the dataset (data not shown), which allowed to estimate the broadband SIF emitted from PSII at all wavelengths ($SIF_{TOT,\lambda}$) by:

$$SIF_{TOT,\lambda} = \frac{SIF_{TOC,760}\cdot f_{PSII}}{f_{esc}}\cdot\frac{v_1(\lambda)}{v_1(760)} = \frac{SIF_{TOC,760}\cdot f_{PSII}\cdot f_\lambda}{f_{esc}}, \lambda \in [650, 840\ nm] \quad (5)$$

with λ the wavelength, $v_1(\lambda)$ the first right singular vector from the SVD technique and $f_\lambda = \frac{v_1(\lambda)}{v_1(760)}$. Eq. 5 becomes, after integration over the broadband range of SIF emission and unit conversion:

$$SIF_{TOT} = \pi\sum_{640}^{850} SIF_{TOT,\lambda}\cdot\frac{10^6\cdot10^{-9}\cdot10^{-3}}{h\cdot c\cdot N_a} \quad (6)$$

with h the Planck constant, c the light velocity, N_a the number of Avogadro, $SIF_{TOT,\lambda}$ in mW m^{-2} nm^{-1} sr^{-1}, and SIF_{TOT} in µmol m^{-2} s^{-1}. The factor 10^{-3} converts from milliwatt to watt, 10^{-9} from nanometers to meters, 10^6 from moles to µmol, and π integrates the signal over the hemispherical space.

2.5. Relationship between SIF and GPP

The relationship between measured GPP and total SIF (i.e., GPP_{EC} and SIF_{TOT}) was characterized by fitting a linear and a linear-plateau segmented model (Jonard et al., 2022). This latter allows to identify a breakpoint in the relationship between two variables. Above the threshold, GPP is constant while SIF increases. Below the threshold, GPP and SIF are positively related. The most significant model was selected by using the lowest Akaike information criterion (AIC), which avoids overfitting (Burnham et al., 2002). Moreover, the SIF yield ($SIF_y = \frac{SIF_{TOT}}{APAR}$) and the light-use efficiency of GPP ($LUE = \frac{GPP_{EC}}{APAR}$, where $APAR = f_{APAR}\cdot PAR$ is the absorbed irradiance), were calculated to reduce the effect of canopy structure and to provide a more physiological interpretation of the variability of SIF_{TOT} and GPP_{EC} throughout the growing season (Martini et al., 2022).

2.6. GPP modeling

The MLR model calculates the actual electron transport rate (J_{SIF}) from SIF_{TOT} by (Gu et al., 2019):

$$J_{SIF} = q_L\cdot\frac{\phi_{PSII,max}\cdot(1 + k_{DF})\cdot SIF_{TOT}}{(1 - \phi_{PSII,max})} \quad (7)$$

with q_L the fraction of open PSII centers, $\phi_{PSII,max}$ the maximum photochemical quantum yield, and k_{DF} the ratio between k_D (representing the rate of constitutive heat thermal dissipation) and k_F (representing the rate of fluorescence emission), set to 19 as in Gu et al. (2019). q_L and $\phi_{PSII,max}$ were calculated from leaf-level measurements (see section 2.9).

Modeled GPP (GPP_{SIF}) was determined from J_{SIF} based on the electron requirements for carboxylation and oxygenation processes (Farquhar et al., 1980; Gu et al., 2019):

$$GPP_{SIF} = q_L\cdot\frac{\phi_{PSII,max}\cdot(1 + k_{DF})\cdot SIF_{TOT}}{(1 - \phi_{PSII,max})}\cdot\frac{(C_i - \Gamma^*)}{(4C_i + 8\Gamma^*)} \quad (8)$$

with C_i the CO_2 concentration in substomatal cavities, directly measured at the leaf level (details in section 2.9) and Γ^* the CO_2 compensation point. Γ^* was estimated from the canopy surface temperature (T_{can}; Bernacchi et al., 2001):

$$\Gamma^* = 42.75\cdot exp\left(\frac{37830\cdot(T_{can} - 278.15)}{298.15\cdot R\cdot(T_{can} + 273.15)}\right) \quad (9)$$

where T_{can} was determined from the longwave fluxes:

$$T_{can} = \sqrt[4]{\frac{LW_{out} - (1 - \varepsilon)\cdot LW_{in}}{\varepsilon\cdot\sigma}} \quad (10)$$

with LW_{in} and LW_{out} the longwave downward and outgoing fluxes, ε the far-infrared emissivity set to 0.97 and σ the Stefan-Boltzmann constant.

2.7. Transpiration modeling

The most widely used equation to estimate LE at the ecosystem scale is the Penman-Monteith equation (Maes et al., 2019; Monteith, 1965). This equation models LE under the hypothesis that ecosystem fluxes originate from a single homogeneous plane (i.e., a single 'big-leaf', Knauer et al., 2018):

$$LE = \frac{\Delta\cdot(R_n - G) + \rho_a\cdot c_p\cdot VPD_{can}\cdot G_{aw}}{\Delta + \gamma\cdot\left(1 + \frac{G_{aw}}{G_{sw}}\right)} \quad (11)$$

with Δ the slope of the saturated pressure curve, R_n the net radiation, G the ground heat flux, ρ_a the air density, c_p the heat capacity of dry air, VPD_{can} the vapor pressure deficit at the canopy surface and γ the psychrometric constant. G_{aw} is the aerodynamic conductance for water vapor transport and G_{sw} refers to the canopy surface conductance to water vapor, which includes evaporation from the soil and transpiration from wet vegetation surfaces. VPD_{can} was determined from T_{can} and air relative humidity. The Thom equation (Thom, 1972) was used to determine G_{aw} from wind speed (u) and air friction velocity (u_*):

$$G_{aw} = \left(\frac{u}{u_*^2} + 6u_*^{-0.667}\right)^{-1} \quad (12)$$

G_{sw} (Eq. 11) was determined by using the USO model while neglecting the minimum stomatal conductance (Medlyn et al., 2011, 2017):

$$G_{sw} \cong g_{sw} = 1.6\left(1 + \frac{g_1}{\sqrt{VPD_{leaf}}}\right)\cdot\frac{A_n}{C_s} \quad (13)$$

with g_1 the slope parameter also related to the marginal water cost of

carbon gain (Medlyn et al., 2011), g_{sw} the stomatal conductance to water vapor and A_n the net photosynthesis. VPD_{leaf} and C_s are respectively the VPD and CO_2 concentration at the leaf surface (i.e., within the boundary layer). All variables in Eq. 13 were measured at the leaf level. g_1 was determined by adjusting a nonlinear regression on leaf-level measurements of A_n, C_s, VPD_{leaf} and g_{sw} (see section 2.9), giving $g_1 = 2.28 \pm 0.09$ $kPa^{0.5}$ (Fig. S1). The combination of Eq. 11 - Eq. 13 with A_n replaced by GPP_{SIF} from Eq. 8 and VPD_{leaf} replaced by VPD_{can}, gives G_{sw} and Tr (Tr_{SIF}) from SIF measurements, under the assumption of dry canopy surface. Therefore, days when precipitation was measured and the subsequent 48 h were discarded from the analysis (Knauer et al., 2018). In these conditions, it is assumed that the evaporation is negligible and that LE only corresponds to Tr. Tr_{SIF} was converted from W m^{-2} to mmol m^{-2} s^{-1} using the latent heat of vaporization and the molar mass of H_2O.

2.8. Assessment of edaphic water stress

2.8.1. Relative extractable water

SWC was used to calculate the relative extractable water (REW) which represents the amount of water available for plant uptake in the root zone (Granier et al., 1999). The original equation of Granier et al. (1999) has been modified to weight the amount of available water by the rooting depth within each soil layer, therefore providing a more realistic estimation of the soil water availability in the root zone. The detail of the calculation of REW can be found in the supplementary materials (Text S1).

2.8.2. Relationship with ecosystem physiology

Physiological processes such as carbon assimilation, stomatal closure or SIF emission often show a two steps response to the decrease in soil water availability with a clear transition from non-limiting to limiting soil water conditions from a threshold (Beauclaire et al., 2023; Gourlez de la Motte et al., 2020; Jonard et al., 2022). In this study, soil water-limiting conditions were defined by using the REW threshold from which a decrease in LUE was observed (Reitz et al., 2023). As any other response ration, LUE is strongly affected by changes in the denominator ($APAR$) especially when it is small. Therefore, a logarithmic transformation was used to avoid skewness in the sampling distribution and to linearize the ratio so that LUE is affected equally by changes in $APAR$ or GPP_{EC} (Hedges et al., 1999). A linear and a linear-plateau segmented model were fitted to the log10-transformed daily means of LUE and daily means of REW, and statistical selection was made according to the lowest AIC similarly to the SIF_{TOT}–GPP_{EC} relationship (Jonard et al., 2022; Reitz et al., 2023; Stocker et al., 2018). The linear-plateau segmented model had the lowest AIC and the REW threshold (REW_{th}) was determined as the corresponding REW below which a decrease in REW induced a decrease in LUE. A threshold of 0.57 ± 0.06 was found (Fig. S2). This lower limit of this threshold (i.e., $REW_{th} = 0.51$) was used to discuss the impact of non-limiting (i.e., $REW > REW_{th}$) or limiting (i.e., $REW < REW_{th}$) soil water conditions on MLR-USO model robustness and on the SIF_{TOT}– GPP_{EC} relationship.

2.9. Gas exchange and fluorescence measurements at the leaf level

q_L, $\phi_{PSII,max}$, C_i and f_{PSII} used in Eq. 1 and Eq. 8, as well as A_n, C_s, and VPD_{leaf} in Eq. 13 were determined from active fluorescence and gas exchange measurements at the leaf level by using a LICOR LI-6400 device and a LI-6400-40 fluorescence chamber (LI-COR Inc., Lincoln, NE, USA). The following procedure was applied to each measurement. Only the youngest and most exposed leaves on the upper part of the canopy were selected, considering that they mostly contributed to the total emitted SIF signal due to their very large role in PAR interception, and their high content in chlorophyll and nitrogen (Li et al., 2015). In the chamber, the CO_2 concentration was set to 400 ppm, and the air humidity and temperature were maintained at ambient level. For the measurements on dark-adapted materials, the actinic light was turned off for at least 20 min. A multiphase fluorescence flash of 9000 µmol m^{-2} s^{-1} was then applied to measure the maximum and minimum fluorescence intensities in the dark (F_m and F_0). After this, the actinic light was turned on and the PAR in the chamber (PAR_{leaf}) was set to ambient level. After stabilization of the fluorescence and gas exchange signal, the steady state fluorescence intensity (F_s) was measured before the application of the same multiphase fluorescence flash to measure the maximum fluorescence intensity under the light (F_m'). The minimum fluorescence of a light-adapted sample (F_0') was measured after the application of a far-red pulse to excite PSI and draw the electrons from PSII to ensure that reaction centers remain fully oxidized. In addition, A_n, leaf transpiration, leaf temperature (T_{leaf}) and C_s were measured. These variables were used to calculate g_{sw}, C_i and VPD_{leaf}. Leaf-level measurements were performed at different locations within the FloX footprint between 7am and 5pm. A total of 387 measurements were collected between April 14 and June 30, 2022 (Fig. 2). These fluorescence intensities should correspond only to PSII emission. This has been considered by hypothesizing that steady-state PSI fluorescence represents 24% of F_s (i.e., $F_{s,PSI} = 0.24\,F_s$) when performing active fluorescence measurements at the leaf level (Pfündel et al., 2013). This contribution reaches 45% in the NIR for SIF in the O_2-A band (i.e., $F_{s,PSI,NIR} = 0.45\,F_s$; Pfündel, 2021). Therefore, q_L, $\phi_{PSII,max}$ and f_{PSII} were calculated as following (Kramer et al., 2004; Jia et al., 2023):

$$q_L = \frac{(F_m' - F_s)\cdot(F_0' - F_{s,PSI})}{(F_m' - F_0')\cdot(F_s - F_{s,PSI})} \tag{14}$$

$$\phi_{PSII,max} = \frac{(F_m - F_0)}{F_m - F_{s,PSI}} \tag{15}$$

$$f_{PSII} = \frac{F_s - F_{s,PSI,NIR}}{F_s} = 1 - \frac{F_{s,PSI,NIR}}{F_s} \tag{16}$$

It is necessary to interpolate MLR model parameters determined by leaf-level measurements campaigns (q_L, $\phi_{PSII,max}$, C_i and f_{PSII}) to calculate GPP_{SIF} (Eq. 8) and Tr_{SIF} (Eq. 11) at a half-hourly timescale before validation. This temporal interpolation has been carried out using the relationship between model parameters and potential environmental drivers (VPD_{leaf}, T_{leaf}, PAR_{leaf}, REW). An exponential model was used to represent the relationship between q_L and PAR_{leaf} (Chang et al., 2021). As C_i is sensitive to leaf temperature with a peak between 20 °C and 30 °C for wheat (Huang et al., 2021), a second-order polynomial model was used to interpolate C_i with T_{leaf}. f_{PSII} was linearly related to PAR_{leaf} by a first-order polynomial model. The equations are:

$$q_L = a_{qL}\cdot exp^{-b_{qL}\cdot PAR_{leaf}} + c_{qL} \tag{17}$$

$$f_{PSII} = a_{fPSII}\cdot PAR_{leaf} + b_{fPSII} \tag{18}$$

$$C_i = a_{Ci}\cdot T_{leaf}^2 + b_{Ci}\cdot T_{leaf} + c_{Ci} \tag{19}$$

q_L, f_{PSII} and C_i were grouped in PAR_{leaf}, T_{leaf} and VPD_{leaf} classes with an interval of respectively 50 µmolm^{-2} s^{-1}, 2 °C and 0.1 kPa before fitting the exponential and polynomial models. Statistical significance of models was evaluated by comparing the AIC of the exponential (Eq. 17) and polynomial (Eq. 18, Eq. 19) models with the AIC of a linear (for Eq. 17, Eq. 19) and a zero-slope model (for Eq. 18). Only models with the lowest AIC are presented. The relationship between model parameters and other potential drivers (i.e., REW, PAR_{leaf}, T_{leaf} and VPD_{leaf}) was also tested (Fig. S3, Table S3).

2.10. Energy partitioning at the leaf level

As mentioned in the introduction, NPQ, SIF and PQ are in competition for solar irradiance. Therefore, the sum of the corresponding

quantum yields (ϕ_{NPQ}, ϕ_{SIF} and ϕ_{PQ}) equals 1 (Porcar-Castell et al., 2014), and the relationship between carbon assimilation and fluorescence at the leaf level is tightly coupled to the dissipation of excessive energy by heat. It is then expected that the partitioning between ϕ_{NPQ}, ϕ_{SIF} and ϕ_{PQ} directly impacts the relationship between SIF_{TOT} and GPP_{EC}. The quantum yields were calculated following (Gu et al., 2019; Jia et al., 2023; Kramer et al., 2004):

$$\phi_{PQ} = \frac{F_m^{'} - F_s}{F_m^{'} - F_{s,PSI}} \tag{20}$$

$$\phi_{NPQ} = \frac{F_s - F_{s,PSI}}{F_m^{'} - F_{s,PSI}} - \frac{F_s - F_{s,PSI}}{F_m - F_{s,PSI}} \tag{21}$$

$$\phi_{SIF} = \frac{1 - \phi_{PSII,max}}{(1 + k_{DF})\left((1 + NPQ)\left(1 - \phi_{PSII,max}\right) + q_L \phi_{PSII,max}\right)} \tag{22}$$

where $NPQ = \frac{F_m - F_m^{'}}{F_m^{'} - F_{s,PSI}}$ is the NPQ parameter. Note that ϕ_{PQ} and ϕ_{NPQ} were corrected for PSI emission and that ϕ_{SIF} corresponds to the SIF quantum yield of PSII (Gu et al., 2019). The relationship between ϕ_{PQ}, ϕ_{NPQ}, ϕ_{SIF} and environmental drivers was evaluated using the correlation coefficients, and their corresponding *p*-values.

2.11. Statistical analysis

The performance of the MLR-USO model was evaluated by calculating the R^2 and the relative root mean square error (rRMSE) between GPP_{SIF}–GPP_{EC} and between Tr_{SIF}–Tr_{EC}, at both daily and half-hourly timescales. The rRMSE was calculated by dividing the root mean square error by the amplitude of EC data (i.e., the difference between the maximum and minimum value). The heteroskedasticity was assessed by calculating the p-value of the Breusch-Pagan test (Breusch and Pagan, 1979) to characterize a potential trend in residuals variability with GPP_{SIF} or Tr_{SIF}. Finally, the relationship between model residuals and potential drivers (REW, VPD_{can}, T_{can}, f_{esc}) was evaluated using the correlation coefficients, and their corresponding p-values.

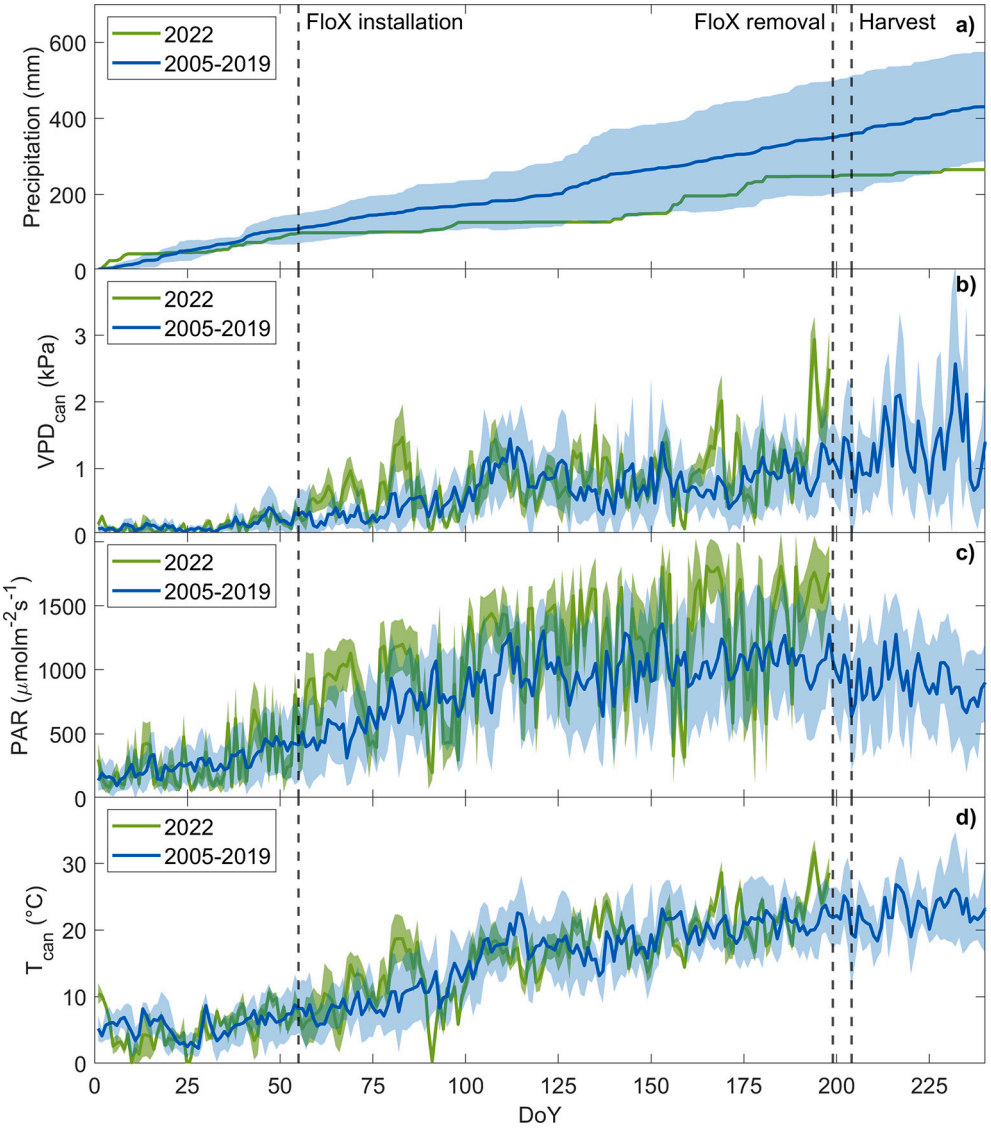

Fig. 1. Temporal evolution in 2022 of daily cumulative precipitation (panel a), canopy vapor pressure deficit (VPD_{can} – panel b), solar irradiance (PAR – panel c) and canopy temperature (T_{can} – panel d) compared to previous winter wheat growing seasons (2005–2019). Shaded areas correspond to the standard deviation around the daily means.

3. Results

3.1. Meteorological conditions and EC fluxes

CO_2, H_2O fluxes and meteorological variables in 2022 were compared to the previous winter wheat growing seasons at BE-Lon by combining the FLUXNET2015 and the ICOS Carbon Portal datasets over the years 2005, 2007, 2009, 2011, 2013 and 2019 (Dumont et al., 2023; Pastorello et al., 2020). The temporal evolution of cumulative precipitation, VPD_{can}, PAR and T_{can} in 2022 is presented in Fig. 1 and was compared to the average values over the reference period 2005–2019. In 2022, several episodes with very low precipitation can be observed, as highlighted by numerous horizontal lines on the cumulative precipitation curve (Fig. 1-a). At the harvest, the total cumulative precipitation in 2022 was about 251 mm, which is not significantly lower than the average cumulative precipitation for the reference period 2005–2019 (361 ± 153 mm).

Four peaks of VPD_{can} were observed in 2022 around DOY 83, 135, 169, 194, clearly above the average values of the reference period (Fig. 1-b). These sharp increases in VPD_{can} also corresponds to an increase in T_{can} and PAR (Fig. 1-c,d). The lack of precipitation during spring and summer 2022 caused a decrease in *REW* between DOY 55 to 85, DOY 98 to 139, and DOY 160 to 173 (Fig. 2-c). The most severe precipitation shortage episode was between DOY 98 to 139, which corresponds to more than 40 days without precipitation. During this period, REW decreased to a minimum value of 0.24. The lowest REW value was 0.14 at DOY 197 (Fig. 2-c). GPP_{EC} and LE_{EC} showed a strong seasonal pattern with a typical bell-shape curves in parallel with canopy cover development and *NDVI* dynamics (Fig. 2-a,b; Fig. 3-a). Maximum values of 55.0 µmol m^{-2} s^{-1} for GPP_{EC} and 419 W m^{-2} for LE_{EC} were observed at DOY 133 (Fig. 2-a,b).

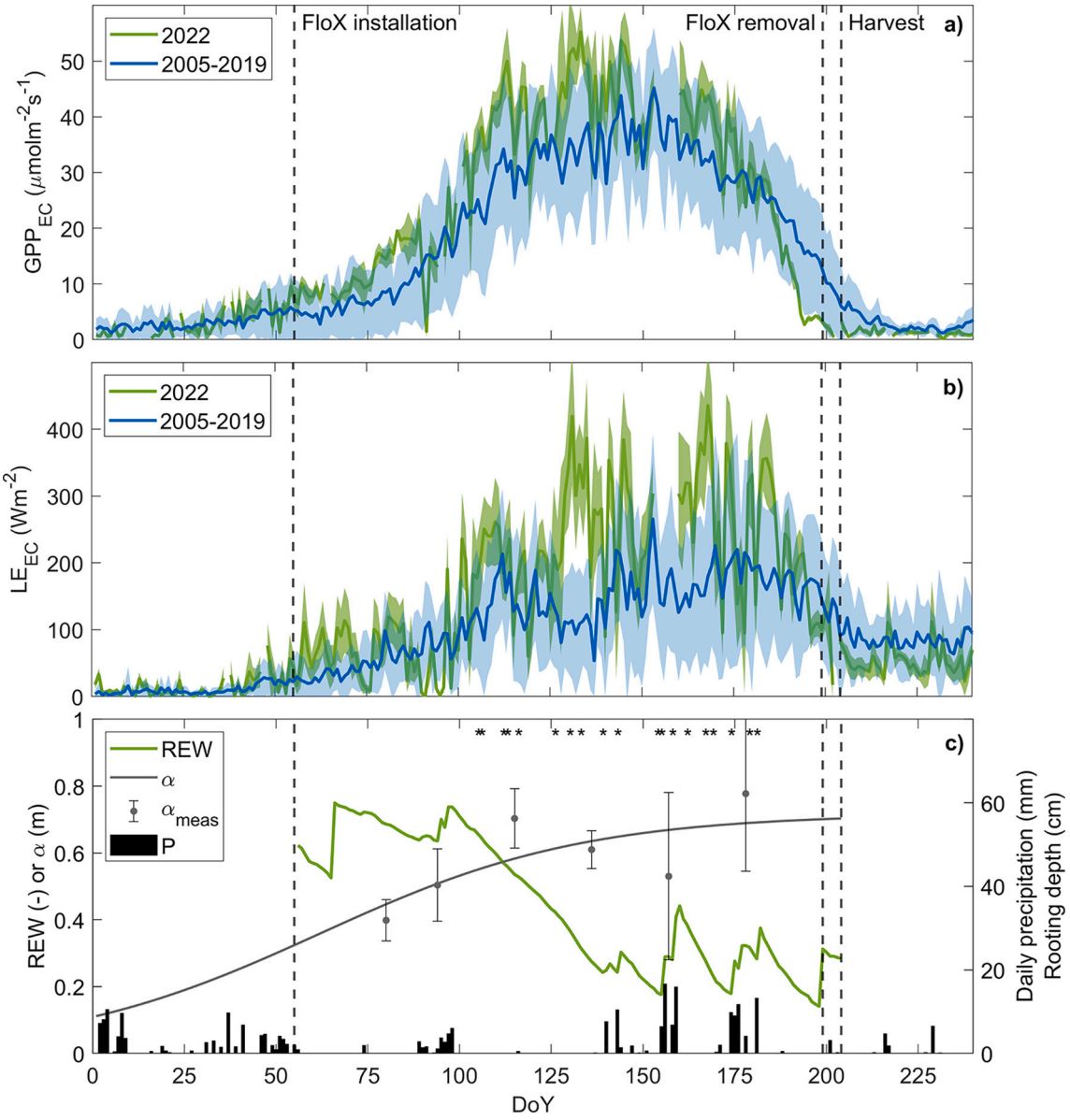

Fig. 2. Temporal evolution in 2022 of gross primary production (GPP_{EC} – panel a), latent heat flux (LE_{EC} – panel b) and relative extractable water (*REW* – panel c). Subplot c) also displays maximum rooting depth measurements (α_{meas}) and extrapolated values (α), as well as daily cumulative precipitation (P) and days when leaf-level measurements were performed (*). Panels a) and b) also display GPP_{EC} and LE_{EC} over the previous winter wheat growing seasons (2005–2019). Shaded areas correspond to the standard deviation around the daily means. The details of the calculation of REW are given in Text S1.

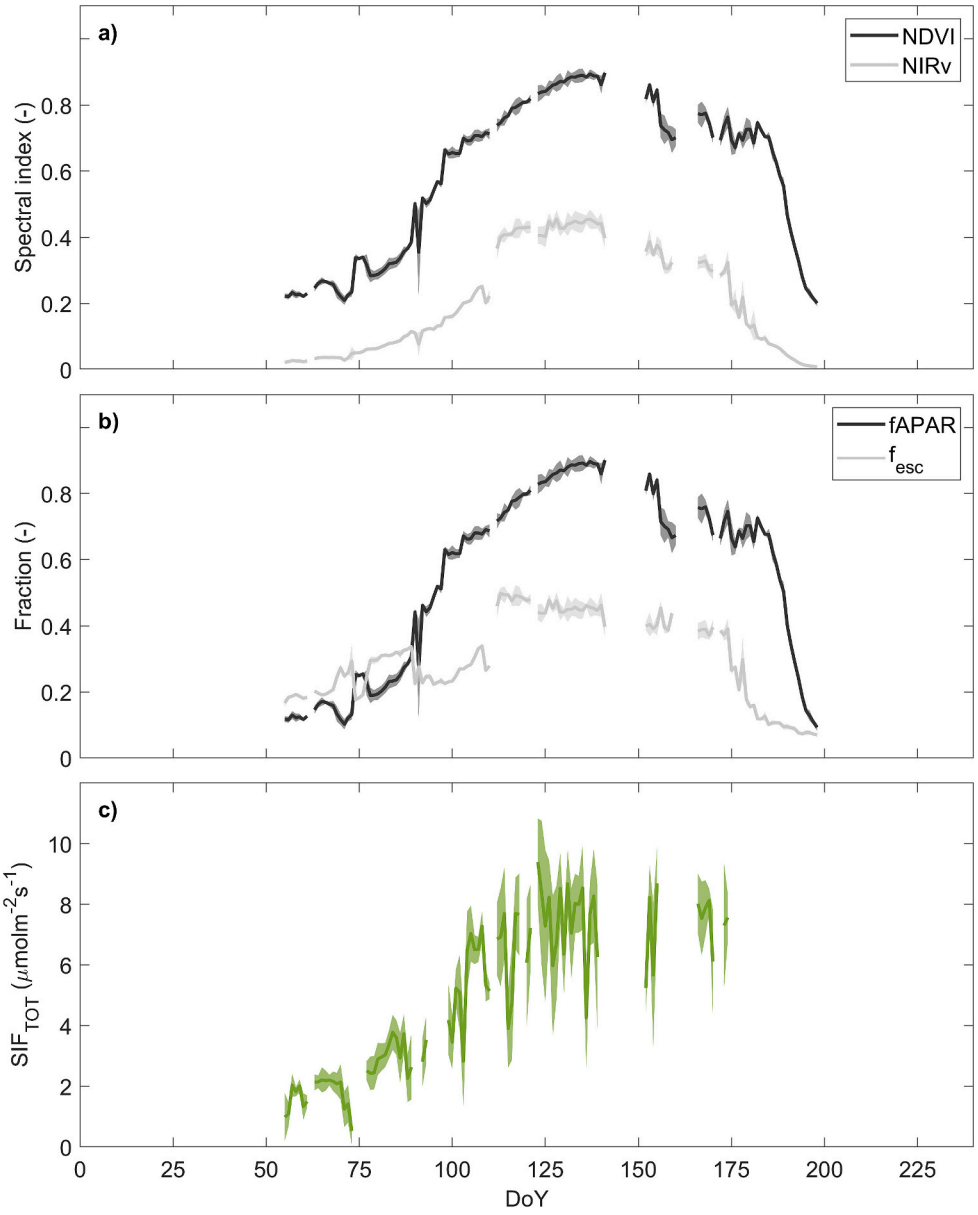

Fig. 3. Temporal evolution in 2022 of daily means of normalized difference vegetation index (*NDVI*) and near-infrared reflectance of vegetation (NIR_v – panel a), fraction of absorbed irradiance (f_{APAR}), escape probability (f_{esc} – panel b), and total sun-induced chlorophyll fluorescence (SIF_{TOT} – panel c). Shaded areas correspond to the standard deviation around the daily means.

3.2. Temporal evolution of proximal sensing data and relationship between SIF and GPP

Due to a malfunction of the QEPro spectrometer after DOY 175, only SIF data from DOY 55 to DOY 175 were analyzed. Moreover, data gaps between DOY 141–152 and 159–166 were caused by sensor maintenance (Fig. 3), and errant *NDVI* data between DOY 98 and 110 were replaced by data from the *NDVI* sensor installed on the EC station (laboratory-made sensor, see Soudani et al. (2012) for references). *NDVI*, NIR_v and f_{APAR} followed vegetation development with a gradual increase from DOY 55 to DOY 130 and a maximum value of respectively 0.89, 0.50 and 0.89 (Fig. 3-a,b), which characterizes the full development of the canopy. A progressive decrease due to senescence and yellowing can be observed from DOY 182 to DOY 198. The variability of f_{esc} was high before DOY 80, corresponding to the beginning of the growing season. Indeed, f_{esc} is very sensitive to short scale variations of NDVI (Eq. 2, Eq. 3). This latter showed a strong variability in the early stage of vegetation growth, which can be explained by the impact of soil reflectance and canopy scattering on the NDVI measurements. Therefore, NDVI measurements are very sensitive to changes in canopy structural proprieties (i.e., such as leaf angle inclination) when vegetation cover is low (Atherton et al., 2022). This might explain the erratic pattern of f_{esc} before DOY 80. From DOY 80, f_{esc} followed crop phenology as NDVI and NIR_v increased, with values stabilizing between 0.50 and 0.39 (Fig. 3-b), which has already been observed in similar crops (Dechant et al., 2020). SIF_{TOT} was impacted by both canopy cover development and half-hourly variations of meteorological conditions (Fig. 3-c). In particular, SIF_{TOT} gradually increased from DOY 55 to a maximum value of 9.34 μmol m^{-2} s^{-1} observed at DOY 123 (Fig. 3-c).

The relationship between GPP_{EC} and SIF_{TOT} was characterized by an increase in GPP_{EC} for $SIF_{TOT} < 6.90$ μmol m^{-2} s^{-1} before a progressive stabilization of GPP_{EC} at ~45.6 μmol m^{-2} s^{-1} for $SIF_{TOT} > 6.90$ μmol m^{-2} s^{-1} (Fig. 4-a). The nonlinearity was observed at very high APAR (~1500 μmol m^{-2} s^{-1}, corresponding to 3.6% of the APAR dataset)

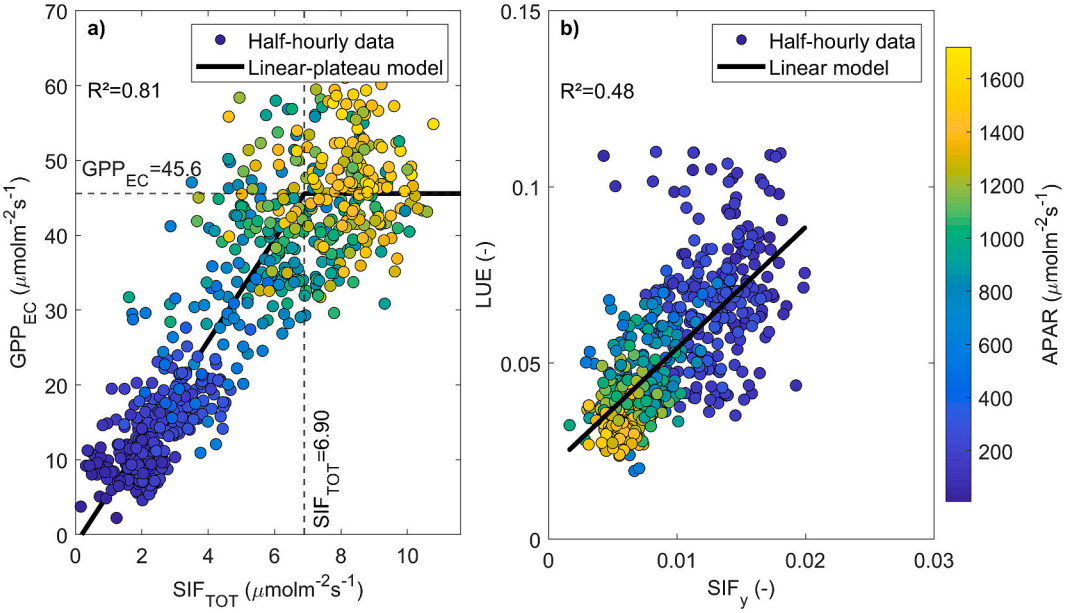

Fig. 4. Relationship between gross primary production (GPP_{EC}) and total sun-induced fluorescence (SIF_{TOT} – panel a), and between light-use efficiency of GPP (LUE) and SIF yield (SIF_y – panel b). The color map indicates the range of absorbed PAR (APAR). R^2 is the coefficient of determination of the linear or linear-plateau segmented model. The selected model was the one with the lowest Akaike information criterion (AIC).

which may suggest a decoupling between GPP_{EC} and SIF_{TOT} induced by light absorption and/or canopy structure effects on the GPP_{EC}–SIF_{TOT} relationship. The relationship between *LUE* and SIF_y was linear (Fig. 4-b), which highlights that the saturating shape was explained by light absorption rather than structural changes (Fig. 4-b). Finally, soil water-limiting conditions (i.e., $REW<REW_{th}$) did not induce a nonlinear pattern between SIF_y and LUE (Fig. 5).

3.3. Leaf-level measurements

T_{leaf} explained a larger part of the variability of C_i compared to VPD_{leaf} and PAR_{leaf} (i.e., highest R^2, Fig. 6, Fig. S3, Table S3). $\phi_{PSII,max}$ remained constant and was not affected by any environmental variables ($\bar{\phi}_{PSII,max} = 0.81$, Fig. S3). q_L exponentially decreased from 0.63 before stabilizing to 0.38 when PAR exceeded ~500 μmol m^{-2} s^{-1} (Fig. 6-a), and f_{PSII} linearly decreased between 0.71 and 0.60 (Fig. 6-b). C_i decreased with increasing T_{leaf} up to ~20 °C before stabilizing above ~20 °C (Fig. 6-c). Fitted coefficients and R^2 (Eq. 17,18 and 19) are given in Table S3. No significant relationship between q_L, f_{PSII} and other environmental drivers was observed (Fig. S3). These equations were used to calculate q_L, C_i and f_{PSII} at the half-hourly timescale using T_{can} (Eq. 10) and PAR for estimating GPP_{SIF} from SIF_{TOT} (Eq. 8). Time series of measurements of model parameters are shown in Fig. S4.

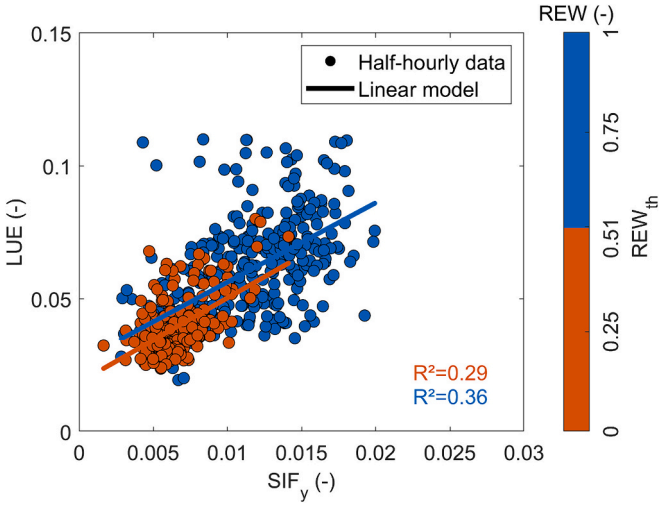

Fig. 5. Relationship between light-use efficiency of photosynthesis (*LUE*) and SIF yield (SIF_y) with relative extractable water (REW). R^2 is the coefficient of determination of the linear model. The color map indicates the range of REW and is defined according to the REW threshold characterizing soil water-limiting conditions (REW_{th}).

A positive correlation between PAR and ϕ_{NPQ} was observed (Fig. 7), where ϕ_{NPQ} increased with PAR from ~0 to ~0.6. On the other hand, ϕ_{PQ} decreased with increasing PAR from ~0.8 to ~0.3, which resulted in a negative correlation (Fig. 7). A weaker negative correlation between ϕ_{SIF} and PAR was also evidenced (Fig. 7). A significant correlation was also observed between leaf-level quantum yields and T_{leaf} and VPD_{leaf} (Fig. S5). In particular, the decrease in ϕ_{SIF} and ϕ_{PQ} with T_{leaf} and VPD_{leaf} was associated to the corresponding increase in ϕ_{NPQ}. Moreover, the decrease in REW did not affect leaf-level quantum yields (Fig. S5).

3.4. MLR-USO model performances for estimating GPP and transpiration

The MLR-USO model reproduced a large proportion of the temporal variability of GPP_{EC} and Tr_{EC} throughout the growing season and under various meteorological conditions (Fig. 8). These results are confirmed by the direct comparison between modeled GPP and Tr (GPP_{SIF} and Tr_{SIF}) and EC measurements (Fig. 9 and Fig. 10). The MLR-USO model explained 95% of the variance of GPP_{EC} at the half-hourly timescale (R^2 = 0.95) with a rRMSE of 13.7% and a slope of the linear regression between GPP_{EC} and GPP_{SIF} close to 1 (Fig. 9-a). At the daily timescale, the rRMSE was slightly lower, while the other statistics remained very similar (R^2 = 0.95, rRMSE = 11.5%, slope = 0.97 ± 0.04) (Fig. 9-b). At the half-hourly timescale, 95% of the variance of Tr_{EC} was explained by the model (R^2 = 0.95) with a rRMSE of 9.1% and a slope of 0.89 ± 0.02 (Fig. 10-a). Similar statistics were observed at the daily timescale (Fig. 10-b). Low REW induced an underestimation of Tr_{SIF} compared to Tr_{EC}, which was more pronounced at the half-hourly timescale (Fig. 10). No deviation from the 1:1 line as APAR increased can be observed for both GPP and Tr (Fig. 9 and Fig. 10). The mean of residuals was very

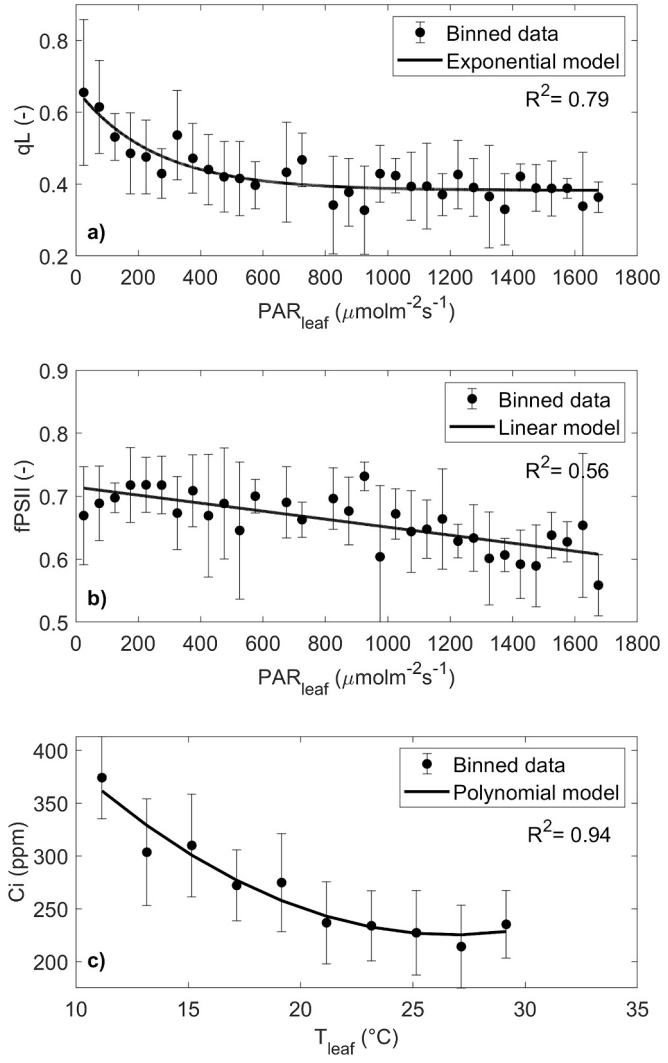

Fig. 6. Relationship between the fraction of open PSII centers (q_L) and the fraction of PSII fluorescence emission (f_{PSII}) with solar irradiance at the leaf level (PAR_{leaf} – panels a and b). Panel c) displays the relationship between CO_2 concentration in substomatal cavities (C_i) and leaf temperature (T_{leaf}). Measurements are grouped into PAR_{leaf} or T_{leaf} classes with an interval of respectively 50 μmolm^{-2} s^{-1} and 2 °C. The error bars show the standard deviation around the mean for each class. R^2 is the coefficient of determination of the exponential or polynomial models.

close to 0 for GPP (0.36 μmol m^{-2} s^{-1} half-hourly / 0.63 μmol m^{-2} s^{-1} daily) and Tr (−0.11 mmol m^{-2} s^{-1} half-hourly / -0.15 mmol m^{-2} s^{-1} daily). An increase in residuals variability as GPP_{SIF} and Tr_{SIF} increased was observed, but only at the half-hourly timescale for GPP (i.e., $p <$ 0.05, Fig. 9 and Fig. 10). GPP residuals were significantly correlated with REW, T_{can} and VPD_{can} but not with f_{esc} (Fig. 11-a,b,c,d). Similar correlations are observed for Tr residuals (Fig. 11-e,f,g,h). More specifically, the correlation was positive between model residuals and REW, and negative for T_{can} and VPD_{can}. A more important trend towards negative residuals for Tr was observed when REW was lower than REW_{th}, which can explain the slight underestimation of Tr_{SIF} compared to Tr_{EC} (Fig. 10). No correlation was observed at the daily timescale for any GPP or Tr residuals.

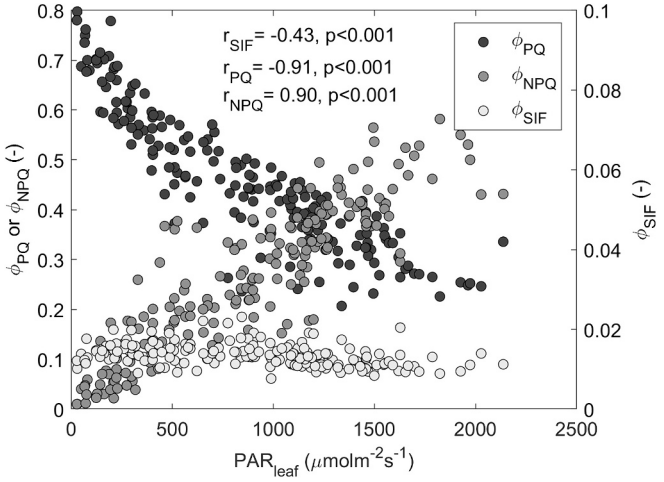

Fig. 7. Relationship between quantum yields of fluorescence (ϕ_{SIF}), non-photochemical quenching (ϕ_{NPQ}) and photochemical quenching (ϕ_{PQ}) with solar irradiance at the leaf level (PAR_{leaf}). r is the correlation coefficient and p is the corresponding p-value.

4. Discussion

4.1. Relationship between MLR-USO model parameters and environmental drivers

A key step for applying the MLR model is the determination of the factors for estimating SIF_{TOT} from $SIF_{TOC,760}$. This step includes the conversion of photosystem-level SIF emission to canopy level, the conversion of narrowband SIF to broadband SIF considering a physiological and structural component, and finally the exclusion of PSI fluorescence. f_λ is constant and does not vary with meteorological variables while f_{esc} integrates the structural changes in the canopy and was retrieved from NIR_V and f_{APAR}, which are both reflectance-based measurements available at local and large scales (Zeng et al., 2019; Dechant et al., 2022). As the SIF signal includes the contribution of both photosystems in the O_2-A band, the effects of PSI cannot be neglected. f_{PSII} was estimated by excluding the contribution of PSI to leaf-level fluorescence intensities which was set to 45% of F_s (Pfündel, 2021). Although this value is higher than previous observations (e.g., Franck et al., 2002; Genty et al., 1990; Pfündel et al., 2013), it can be used to consider PSI contribution in the O_2-A band as it was calculated from selective fluorescence measurements above 700 nm (Pfündel, 2021; Jia et al., 2023). f_{PSII} moderately decreased with PAR, while being not affected by the increase in VPD_{leaf}, T_{leaf} or REW (Fig. 6, Fig. S3). This dynamic is similar to the PAR - ϕ_{SIF} relationship which showed a week negative correlation (Fig. 7) and can be explained by a strong coupling between F_s and PQ quantum yield under high irradiance when NPQ is limiting (Maguire et al., 2020; Liu et al., 2022a, 2022b). This contrasts with other studies which modeled the fluorescence quantum yields ratio (Eq. 16) with temperature, PAR and CO_2 availability, making f_{PSII} highly sensitive to other environmental conditions (Liu et al., 2022a, 2022b; Bacour et al., 2019; van der Tol et al., 2014). Disentangling the importance of PSI contribution in the total SIF signal is one important issue to be considered in future studies (Porcar-Castell et al., 2021), as it directly influences the magnitude of SIF_{TOT} especially in the O_2-A band.

Given the wide diversity in physiological mechanisms across ecosystems, it is expected that the parameters of the MLR-USO model (i.e., $\varphi_{PSII,max}$, q_L, C_i and g_1) are to be determined from a PFT-based calibration. We tackled this problem by taking in-situ measurements at the leaf level. T_{leaf} explained the most important part of C_i variability (highest R^2, Fig. 6, Table S3) which is explained by the temperature response of stomata and Rubisco (Warren, 2006). This combined effect leads to a

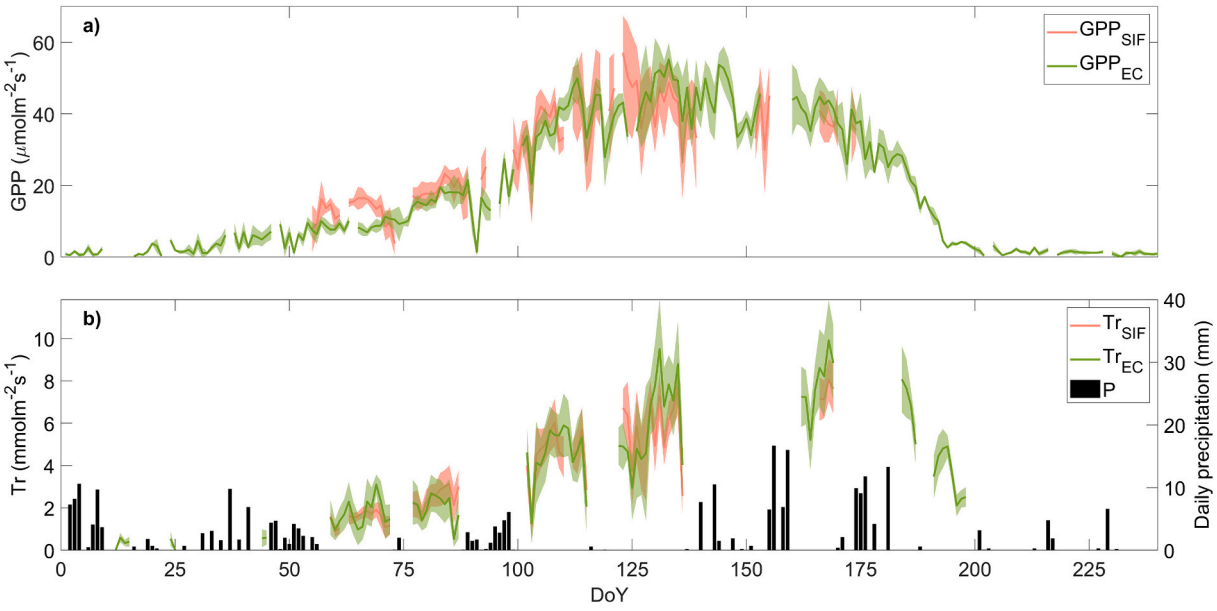

Fig. 8. Temporal evolution in 2022 of gross primary production from eddy covariance (GPP_{EC}) and estimated by the MLR-USO model (GPP_{SIF} – panel a). Panel b) shows the temporal evolution of daily transpiration from eddy covariance (Tr_{EC}) and estimated by the MLR-USO model (Tr_{SIF}), as well as the daily cumulative precipitation (P). Shaded areas correspond to the standard deviation around the daily means.

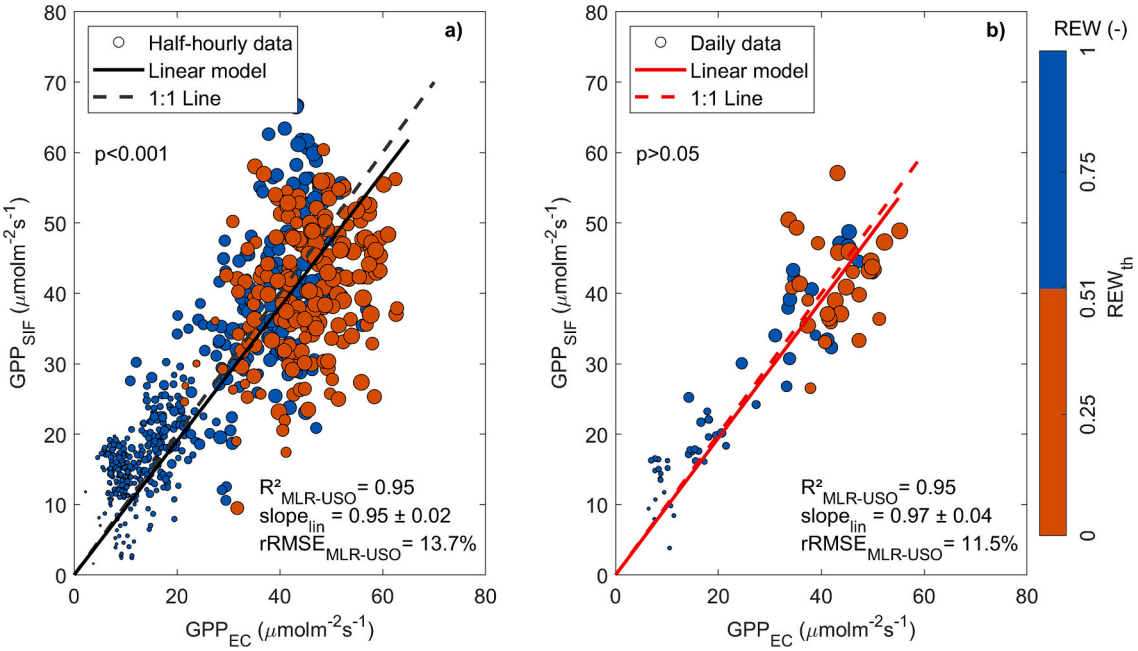

Fig. 9. Scatterplot between gross primary production from eddy covariance (GPP_{EC}) and gross primary production estimated by the MLR-USO model (GPP_{SIF}) at the half-hourly (panel a) and daily (panel b) timescales. Dot size is proportional to the absorbed photosynthetic active radiation (APAR). The color map indicates the range of relative extractable water (REW) and is defined according to the REW threshold characterizing soil water-limiting conditions (REW_{th}). $R^2_{MLR\text{-}USO}$ and $rRMSE_{MLR\text{-}USO}$ are respectively the coefficient of determination and the relative root mean squared error calculated from GPP_{SIF} and GPP_{EC}. $slope_{lin}$ is the slope of the linear relationship between GPP_{SIF} and GPP_{EC}. p is the p-value of the Breusch-Pagan test for heteroskedasticity.

temperature optimum for photosynthesis, typically around 25 °C (Crous et al., 2022), with some variability between species (Marchin et al., 2022). Such relationship was also observed in other studies conducted on winter wheat (Urban et al., 2018; Huang et al., 2021).

The exponential decrease in q_L with PAR illustrates the closure of PSII reaction centers when solar irradiance increases (Cendrero-Mateo et al., 2015; Zivcak et al., 2014; Flexas et al., 2002; Broddrick et al., 2022; Ouzounis et al., 2015). We did not observe an effect of other environmental variables on q_L besides PAR (Fig. S3), in contrast with previous studies which showed a significant effect of heat and atmospheric dryness on this parameter (Han et al., 2022b; Shin et al., 2021; Zhou et al., 2019; Cano et al., 2013). However, it might be possible that our experimental set-up didn't allow the identification of such effects as chlorophyll fluorescence measurements were carried out along with gas exchanges, which limited the number of measurements throughout the day and the growing season. Expanding the range of environmental variables under controlled conditions could uncover such additional effects (e.g., Han et al., 2022b).

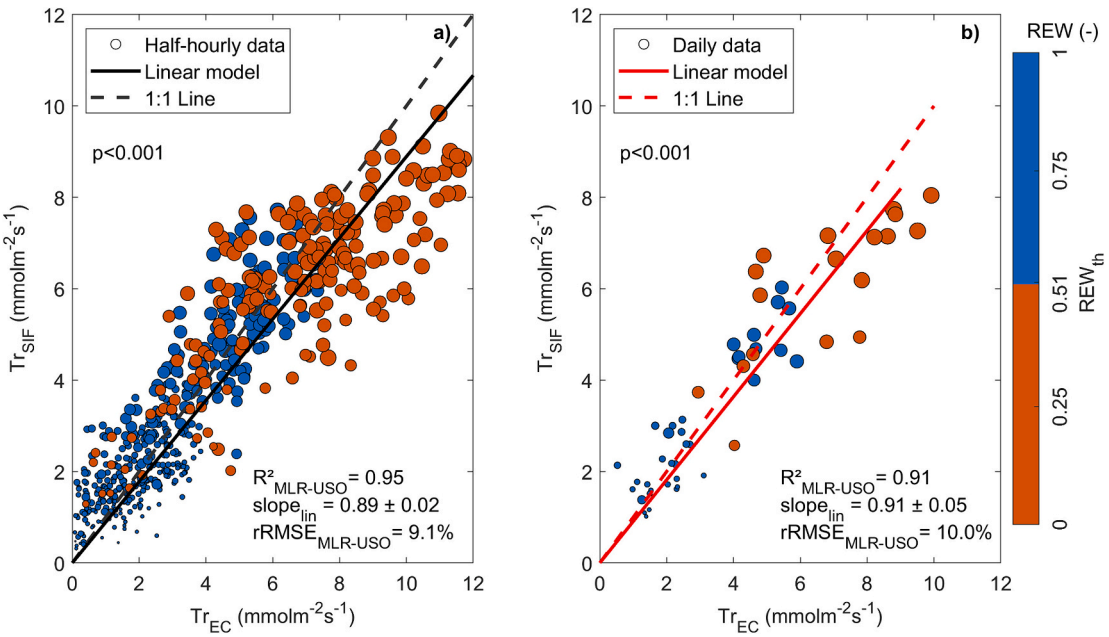

Fig. 10. Scatterplot between transpiration from eddy covariance (Tr_{EC}) and transpiration estimated by the MLR-USO model (Tr_{SIF}) at the half-hourly (panel a) and daily (panel b) timescales. Dot size is proportional to the absorbed photosynthetic active radiation (APAR). The color map indicates the range of relative extractable water (REW) and is defined according to the REW threshold characterizing soil water-limiting conditions (REW_{th}). $R^2_{MLR-USO}$ and $rRMSE_{MLR-USO}$ are respectively the coefficient of determination and the relative root mean squared error calculated from Tr_{SIF} and Tr_{EC}. $slope_{lin}$ is the slope of the linear relationship between Tr_{SIF} and Tr_{EC}. p is the p-value of the Breusch-Pagan test for heteroskedasticity.

4.2. SIF-GPP relationship

The saturation of GPP_{EC} at high SIF_{TOT} (Fig. 4-a) and the linearity between LUE and SIF_y (Fig. 4-b) indicates that APAR is an important driver of the dynamics of GPP_{EC} and SIF_{TOT}. Such relationship has also been observed for croplands, savannas (Yao et al., 2022) or needleleaf forests (Kim et al., 2021; Yao et al., 2022). This nonlinearity can be explained by the competitive mechanism between ϕ_{NPQ}, ϕ_{PQ} and ϕ_{SIF} at the leaf level for the incoming irradiance. We found an asymmetric pattern of ϕ_{PQ} and ϕ_{NPQ} dynamics with PAR (Fig. 7) as highlighted by numerous studies (Baker, 2008; van der Tol et al., 2014; Chen et al., 2019; Gu et al., 2019). In light-limiting conditions, most of the incoming PAR is used for fueling the dark reactions of photosynthesis by carrying the energy through the electron transport chain to produce ATP and NADPH, resulting in a high PQ at low PAR. As more energy is received by chlorophyll molecules, PSII reaction centers close (decrease in q_L) and the rate of absorbed photons decreases (decrease in ϕ_{PQ}). In these conditions, numerous regulatory mechanisms are used to dissipate the excess energy as heat to prevent the formation of reactive oxygen species (see Demmig-Adams and Adams (2006) for a review), resulting in an increase in ϕ_{NPQ} with increasing PAR. As ϕ_{SIF} depends on NPQ and q_L (Eq. 22), the opposite behavior of these two parameters with PAR explains the weaker sensitivity of ϕ_{SIF} to PAR (Fig. 7), and by extension the nonlinearity between SIF_{TOT} and GPP_{EC} at high APAR (Fig. 4-a, Gu et al., 2019).

The linearity between SIF_y and LUE was also observed under soil water-limiting conditions (i.e., REW < REW_{th}, Fig. 5). Similar results were shown in deciduous forests (He et al., 2020; Yang et al., 2015), winter wheat crop (Shen et al., 2022) or natural grassland (Verma et al., 2017). A key factor impacting SIF_y and LUE is the maximum carboxylation rate of Rubisco (V_{cmax}). A decrease in V_{cmax} is often observed in crops during drought (e.g., Beauclaire et al., 2023; Zhou et al., 2013), which could explain the decrease in LUE with REW as highlighted in this study (Fig. S2). Moreover, numerous studies using the SCOPE model (van der Tol et al., 2009) have shown that SIF is sensitive to V_{cmax} (Camino et al., 2019; Koffi et al., 2015; Wang and Xiao, 2021; Zhang et al., 2014, 2016, 2018), suggesting that SIF_y may decrease as well when soil water availability is reduced. Therefore, the linearity between SIF_y and LUE could be explained by a similar sensitivity of LUE and SIF_y to V_{cmax} during water stress.

Unlike the saturation of GPP_{EC} at high $APAR$ and SIF_{TOT} (Fig. 4-a), a linear relationship between GPP_{SIF} and SIF_{TOT} was observed (Fig. S6-d). This suggests that the model did not capture the saturation of GPP_{EC} at high APAR. However, the corresponding impact on model performance was limited as only 3.6% of the APAR data was above the saturation point of ~1500 μmol m^{-2} s^{-1} (section 3.2; Fig. 4-a). In the MLR model, the influence of PAR on GPP_{SIF} is implemented through the effects of q_L on J_{SIF} (Eq. 7, Eq. 17). This sensitivity is explained by the coupling between the dark and light reactions of photosynthesis. In particular, the production of energy-carrier molecules (i.e., ATP and NADPH) by the electron transport chain (which depends on q_L) must balance carbon uptake, itself regulated by the stomatal dynamics (Gu et al., 2019). As SIF_{TOT} is the product of ϕ_{SIF}, f_{esc}, and $APAR$ (Gu et al., 2019), it is expected that SIF_{TOT} increases with PAR. On the other hand, the decrease in q_L (Eq. 17, Fig. 6-a) compensates for the corresponding increase in SIF_{TOT} in the MLR model (i.e., $GPP_{SIF} \approx q_L \cdot SIF_{TOT}$, Eq. 8). As a result, the shape of the PAR–q_L relationship modulates the sensitivity of GPP_{SIF} to SIF_{TOT} (Gu et al., 2019).

The importance of the PAR–q_L relationship on GPP_{SIF} can be assessed by simulating q_L light-response curves based on the 95% confidence intervals of the fitted parameters (Eq. 17, Table S3, Fig. S6-a). These data are then fed into the MLR model (Eq. 8), which gives a modeled GPP ($GPP_{SIF,mod}$) using modeled SIF determined from the light-use efficiency model (i.e., $SIF_{TOT,mod} = \phi_{SIF} \cdot f_{esc} \cdot f_{APAR} \cdot PAR$, where f_{esc} and f_{APAR} are set to constant, and ϕ_{SIF} is estimated from a linear relationship between ϕ_{SIF} and PAR at the leaf level - Fig. 7, Fig. S6). This sensitivity analysis showed that the variability of the PAR–q_L model did not change the pattern of the light response curve of $GPP_{SIF,mod}$, which remained very similar to the PAR–$SIF_{TOT,mod}$ relationship (Fig. S6-b). This similar sensitivity to PAR explained the strong linearity between the two variables regardless of the PAR–q_L response curves (Fig. S6-c). This suggests that the nonlinearity between SIF_{TOT} and GPP_{SIF} is not likely to be

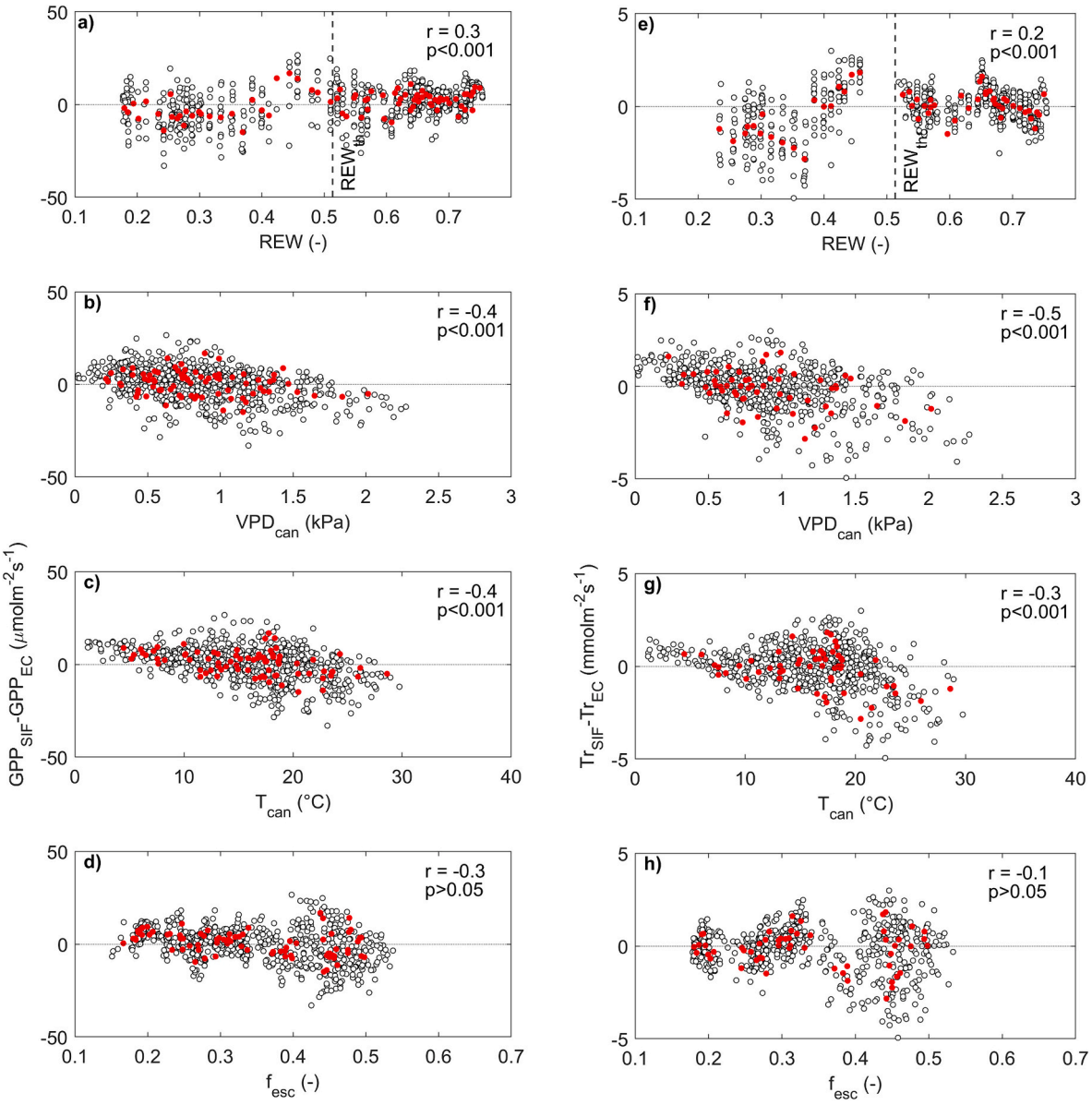

Fig. 11. Scatterplot of MLR-USO model residuals of gross primary production ($GPP_{SIF} - GPP_{EC}$) and transpiration ($Tr_{SIF} - Tr_{EC}$) compared to relative extractable water (REW- panels a, e), canopy vapor pressure deficit (VPD_{can} – panels b, f), canopy temperature (T_{can} – panels c, g) and escape probability (f_{esc} – panels d, h). Dark dots correspond to half-hourly data and red dots to daily data. r is the correlation coefficient and p is the corresponding p-value. (For interpretation of the references to color in this figure legend, the reader is referred to the web version of this article.)

related to the measurements and parameterization of q_L as performed in this study.

One possible explanation of such discrepancy lies in the location of leaf-level measurements within the canopy. In particular, only sunlit leaves at the top of the canopy were selected for active chlorophyll fluorescence measurements, thus implicitly neglecting the contribution of the lower parts of the canopy to the SIF signal. However, wheat canopies can be characterized by leaves with various nitrogen content and structure (Furbank et al., 2015; Chang et al., 2022), and can have an uneven contribution to the observed SIF signal. For instance, while sunlit leaves receive both diffuse and direct light, the proportion of absorbed diffuse light is higher for shaded leaves, which impacts their light absorption proprieties. In-situ measurements have shown that the sensitivity of q_L to PAR changes with the sunlit-shaded status of the leaf (Zivcak et al., 2014; Chang et al., 2021), which is also supported by model simulations on evergreen needleleaf forests (Chen et al., 2024). Such variability could explain the observed saturation of GPP_{SIF} at high PAR at the ecosystem scale. This hypothesis is supported by the sensitivity analysis on q_L conducted beyond the 95% confidence interval of PAR–q_L model parameters (Fig. S7), which shows that q_L is a key parameter for reproducing the SIF-GPP relationship. Neglecting such complexity in the response of a canopy-scale q_L to irradiance may explain the linearity between SIF_{TOT} and GPP_{SIF} at high APAR. This is even more relevant for dense canopies where the performances of the MLR-USO model might be significantly affected under non-limiting light conditions. Future examination of the dependence of q_L on environmental conditions while differentiating light distribution through the canopy is needed (Chen et al., 2024; Chang et al., 2021).

4.3. Performance of the MLR-USO model

4.3.1. Overall performances

The MLR model was used to determine GPP from TOC SIF measurement over a winter wheat crop. For the first time, this model has

been coupled with the USO model for stomatal conductance (Medlyn et al., 2011) to use both stomatal optimality theory and the MLR approach to estimate carbon and water fluxes with a single SIF measurement above the canopy. These findings should be considered in the light of previous studies, which already highlighted the promising capacities of the MLR model for predicting GPP at the canopy scale of an irrigated winter wheat crop (Liu et al., 2022b), at the leaf scale for a grass and two tree species (Shi et al., 2022), or for winter wheat grown under controlled conditions (Jia et al., 2023). Another recent study of Han et al. (2022a) evaluated the robustness of the MLR model at the leaf level for 29 C_3 and C_4 plant species (not including winter wheat) representative of the major PFT across the globe and demonstrated that the MLR model was also capable of estimating net assimilation rate under diverse light and temperature conditions. The direct use of SIF to model Tr was also tested by Feng et al. (2021) who coupled the MLR model with the Ball-Woodrow-Berry (BWB) parameterization for stomatal conductance (Ball et al., 1987). Although Tr estimated from the MLR-BWB model was in a good agreement with EC data for one maize site and two forest sites, the results might have been impacted by neglecting the effects of changes in canopy structure (i.e., setting f_{esc} to constant, Feng et al., 2021). Our study shows that accounting for canopy structural changes and model parameters dependence on environmental variables is critical for estimating GPP and Tr from SIF.

4.3.2. MLR-USO model robustness during dry conditions

The decrease in *LUE* from REW_{th} (Fig. S2) highlights that winter wheat photosynthesis is sensitive to the decrease in soil water availability (Li et al., 2023; Yang et al., 2023), which can lead to yield losses (Riedesel et al., 2023). Statistical metrics indicated that the MLR-USO model performed well even when soil water was limiting (i.e., REW $<$ REW_{th}), or when T_{can} and VPD_{can} were high. The slopes of the linear regressions between MLR-USO model estimates (GPP_{SIF}, Tr_{SIF}) and EC measurements (GPP_{EC}, Tr_{EC}) were very close to one (Fig. 9, Fig. 10), which indicates that the influence of meteorological conditions and changes in canopy structure were reproduced by the model through: (i) the dependence of model parameters on PAR and T_{can}, and (ii) the sensitivity of SIF_{TOT} to VPD_{can} and *REW*.

However, the correlation between model residuals and environmental drivers (T_{can}, VPD_{can} and REW) suggests that soil water-limiting conditions and high T_{can} and VPD_{can} increased the error term of the MLR-USO model. The cone-shaped scatterplot between model residuals and REW (Fig. 11) can be explained by uncertainties in the partitioning of NEE between GPP_{EC} and R_{ECO}. For instance, the partitioning of carbon fluxes from EC data relies on the accuracy of the relationship between T_{air} and R_{ECO} (i.e., nighttime method), which can be affected by soil water availability, diffuse radiation, soil temperature (Wohlfahrt and Galvagno, 2017) or the inhibition of daytime respiration (Keenan et al., 2019). Although GPP_{EC} was retrieved using the ONEFlux pipeline which uses relatively short moving windows to establish the relationship between T_{air} and R_{ECO} (Reichstein et al., 2005; Pastorello et al., 2020), rapid changes in climate conditions such as rewetting after precipitation shortage episodes may induce a strong variability in this relationship, therefore impacting the accuracy of NEE partitioning (Tramontana et al., 2020). This may explain the larger variability and the decreasing trend of the residuals for REW $<$ REW_{th}, as numerous rainfall events were observed around DOY 150 after a constant reduction of soil water availability during the 40-days precipitation shortage period. In addition, MRL-USO parameters and VPD_{can} were determined using T_{can} from far-infrared radiation measurements at the canopy surface. While this approach has the advantage of increasing the versatility of the MLR-USO model for a use at larger scales with RS of land surface temperature (Li et al., 2013; Hulley et al., 2019), the nighttime partitioning method uses T_{air} instead of T_{can} to determine ecosystem respiration and GPP_{EC} from NEE (Reichstein et al., 2005). This difference may increase model residuals, especially when drought affects the coupling between T_{can} and T_{air} (Aprile et al., 2013; Pradhan et al., 2022). The choice of the driving temperature for R_{ECO} and the partitioning of NEE has been discussed in many studies and is still under debate in the scientific community (Lasslop et al., 2012; Wohlfahrt and Galvagno, 2017). A recent paper of Kira et al. (2021) has explored the possibility to use SIF to empirically model GPP to improve the partitioning of NEE. In this perspective, the MLR model also represents a promising perspective to improve the partitioning of NEE by modeling GPP independently from NEE.

Finally, differences between Tr_{SIF} and Tr_{EC} may originate from the calibration of the USO model. g_1 was estimated by using leaf-level measurements of gas exchanges, and the value of 2.28 $kPa^{0.5}$ was in the range of the results of the study of Medlyn et al., 2017 for crops, who calibrated the USO model from EC and leaf-level measurements. In our study, leaf-level measurements were conducted on sunlit leaves at the top of the canopy, which do not integrate the whole canopy variability of plant functional traits and meteorological conditions. In particular, canopy architecture induces variability in sun exposure, resulting in within-canopy gradients of meteorological conditions (Coble et al., 2017) or plant traits (Niinemets et al., 2015). Maximum stomatal conductance and stomatal sensitivity to PAR may be higher in the upper part of the canopy (Van Wittenberghe et al., 2012, Tarvainen et al., 2013) whereas C_i is substantially lower in the deep canopy layers (Niinemets et al., 2004). Therefore, the stomatal sensitivity to photosynthesis (i.e., the paramter g_1) can be influenced by within-canopy variations in environmental conditions (Miner et al., 2017), which ultimately results in uncertainties when scaling from leaves to the canopy. Limiting leaf-level measurements to sunlit leaves in the upper layers of the canopy may not capture such variability and the potential effect of REW on g_1. In particular, it has been shown that g_1 may increase under soil water-limiting conditions at the canopy scale (e.g., Beauclaire et al., 2023; Gourlez de la Motte et al., 2020), which could lead to an underestimation of canopy conductance during soil water stress. Considering this within-canopy variability might be important to model biosphere-atmosphere fluxes for more dense and complex ecosystems such as forests (Bonan et al., 2021). Future efforts should be focused on elucidating the relationship between model parameters and environmental conditions in dense canopies before testing the MLR-USO model over a wider variety of ecosystems.

Despite this uncertainty in the calibration, the MLR-USO model still reproduced a very high proportion of GPP_{EC} and Tr_{EC} variability while no parameters were downregulated by REW. It indicates that SIF_{TOT} was sensitive to the decrease in soil water availability either through changes in the physiological (i.e., $SIF_{TOC,760}$) or structural (i.e., f_{esc}) component of SIF_{TOT}. Although $SIF_{TOC,760}$ may decrease due to an increase in NPQ (Porcar-Castell et al., 2014; Xu et al., 2021), canopy structure through f_{esc} can also be affected by changes in leaf angle distribution usually caused by leaf rolling (Lu et al., 2020; Dechant et al., 2020; Xu et al., 2021) which is a common adaptative response of winter wheat for reducing transpiration and lowering leaf surface temperature during water stress (Ali et al., 2022; Blum and Tuberosa, 2018). Disentangling drought effects between structural or physiological changes would require additional measurements of morphological traits such as leaf angle distribution (Zou et al., 2014; Kattenborn et al., 2022).

5. Conclusion

This study provides a method which combines existing mechanistic modeling frameworks for estimating gross primary production (GPP) and transpiration (Tr) from sun-induced chlorophyll fluorescence (SIF) observations. The novelty of this approach lies in the joint representation of stomatal optimality and light use partitioning processes in a small set of mechanistically-based equations. Our results show that model parameters can be retrieved from canopy temperature and solar irradiance, which are available at large scales from RS data. A high correlation between MLR-USO model estimates and eddy covariance measurements was observed, with more than 90% of variance in observed GPP and Tr explained by the model ($R^2 \geq 0.91$, rRMSE $\leq$ 13.7% for all timescales)

across a wide range of environmental conditions, including light-limiting and soil water-limiting conditions. We also showed that the sensitivity of the fraction of open PSII centers to PAR plays a key role in regulating the response of GPP to SIF. This study confirms that the MLR-USO model can be used for estimating carbon and water fluxes from TOC SIF. More ecosystem-scale studies are needed to fully assess the potential of such model before an application at larger scales with satellite data. This study contributes to paving the way towards an improvement of the modeling of carbon and water fluxes across scales.

CRediT authorship contribution statement

Quentin Beauclaire: Writing – review & editing, Writing – original draft, Visualization, Software, Methodology, Investigation, Formal analysis, Conceptualization. **Simon De Cannière:** Writing – review & editing, Writing – original draft, Resources, Methodology, Formal analysis, Conceptualization. **François Jonard:** Writing – review & editing, Writing – original draft, Validation, Supervision, Resources, Methodology, Formal analysis, Conceptualization. **Natacha Pezzetti:** Investigation, Formal analysis, Conceptualization. **Laura Delhez:** Writing – review & editing, Data curation. **Bernard Longdoz:** Conceptualization, Formal analysis, Investigation, Methodology, Supervision, Validation, Writing – original draft, Writing – review & editing.

Declaration of competing interest

The authors declare that they have no known competing financial interests or personal relationships that could have appeared to influence the work reported in this paper.

Data availability

Data will be made available on request.

Acknowledgments

This research was conducted within the framework of the ICOS Wallonia project, which is supported by the Service Public de Wallonie, Belgium [1217769]. Simon De Cannière was funded by the Deutsche Forschungsgemeinschaft (DFG, German Research Foundation) under Germany's excellence strategy-EXC 2070–390,732,324. The other researchers were funded by the Federation Wallonie Bruxelles (FWB). The Fluorescence boX (FloX) was provided by the Forschungszentrum Jülich.

Appendix A. Supplementary data

Supplementary data to this article can be found online at https://doi.org/10.1016/j.rse.2024.114150.

References

Ali, Z., Merrium, S., Habib-ur-Rahman, M., Hakeem, S., Saddique, M.A.B., Sher, M.A., 2022. Wetting mechanism and morphological adaptation; leaf rolling enhancing atmospheric water acquisition in wheat crop—a review. Environ. Sci. Pollut. Res. 29, 30967–30985. https://doi.org/10.1007/s11356-022-18846-3.

Aprile, A., Havlickova, L., Panna, R., Marè, C., Borrelli, G.M., Marone, D., Perrotta, C., Rampino, P., De Bellis, L., Curn, V., Mastrangelo, A.M., Rizza, F., Cattivelli, L., 2013. Different stress responsive strategies to drought and heat in two durum wheat cultivars with contrasting water use efficiency. BMC Genomics 14, 821. https://doi.org/10.1186/1471-2164-14-821.

Atherton, J., Zhang, C., Oivukkamäki, J., Kulmala, L., Xu, S., Hakala, T., Honkavaara, E., MacArthur, A., Porcar-Castell, A., 2022. What does the NDVI really tell us about crops? Insight from proximal spectral Field sensors. In: Bochtis, D.D., Lampridi, M., Petropoulos, G.P., Ampatzidis, Y., Pardalos, P. (Eds.), Information and Communication Technologies for Agriculture—Theme I: Sensors. Springer International Publishing, Cham, pp. 251–265. https://doi.org/10.1007/978-3-030-84144-7_10.

Bacour, C., Maignan, F., MacBean, N., Porcar-Castell, A., Flexas, J., Frankenberg, C., Peylin, P., Chevallier, F., Vuichard, N., Bastrikov, V., 2019. Improving estimates of Gross primary productivity by assimilating solar-induced fluorescence satellite retrievals in a terrestrial biosphere model using a process-based SIF model. J. Geophys. Res. Biogeosci. 124, 3281–3306. https://doi.org/10.1029/2019JG005040.

Badgley, G., Field, C.B., Berry, J.A., 2017. Canopy near-infrared reflectance and terrestrial photosynthesis. Sci. Adv. 3, e1602244 https://doi.org/10.1126/sciadv.1602244.

Baker, N.R., 2008. Chlorophyll Fluorescence: A Probe of Photosynthesis In Vivo. Annu. Rev. Plant Biol. 59, 89–113. https://doi.org/10.1146/annurev.arplant.59.032607.092759.

Baldocchi, D., 2014. Measuring fluxes of trace gases and energy between ecosystems and the atmosphere - the state and future of the eddy covariance method. Glob. Chang. Biol. 20, 3600–3609. https://doi.org/10.1111/gcb.12649.

Ball, J.T., Woodrow, I.E., Berry, J.A., 1987. A model predicting stomatal conductance and its contribution to the control of photosynthesis under different environmental conditions. In: Biggins, J. (Ed.), Progress in Photosynthesis Research: Volume 4 Proceedings of the VIIth International Congress on Photosynthesis Providence, Rhode Island, USA, August 10–15, 1986. Springer Netherlands, Dordrecht, pp. 221–224. https://doi.org/10.1007/978-94-017-0519-6_48.

Beauclaire, Q., Heinesch, B., Longdoz, B., 2023. Non-stomatal processes are responsible for the decrease in gross primary production of a potato crop during edaphic drought. Agric. For. Meteorol. 343, 109782 https://doi.org/10.1016/j.agrformet.2023.109782.

Beer, C., Reichstein, M., Tomelleri, E., Ciais, P., Jung, M., Carvalhais, N., Rödenbeck, C., Arain, M.A., Baldocchi, D., Bonan, G.B., Bondeau, A., Cescatti, A., Lasslop, G., Lindroth, A., Lomas, M., Luyssaert, S., Margolis, H., Oleson, K.W., Roupsard, O., Veenendaal, E., Viovy, N., Williams, C., Woodward, F.I., Papale, D., 2010. Terrestrial Gross carbon dioxide uptake: global distribution and covariation with climate. Science 329, 834–838. https://doi.org/10.1126/science.1184984.

Bernacchi, C.J., Singsaas, E.L., Pimentel, C., Portis Jr., A.R., Long, S.P., 2001. Improved temperature response functions for models of rubisco-limited photosynthesis: *in vivo* rubisco enzyme kinetics. Plant Cell Environ. 24, 253–259. https://doi.org/10.1111/j.1365-3040.2001.00668.x.

Blum, A., Tuberosa, R., 2018. Dehydration survival of crop plants and its measurement. J. Exp. Bot. 69, 975–981. https://doi.org/10.1093/jxb/erx445.

Boas, T., Bogena, H., Grünwald, T., Heinesch, B., Ryu, D., Schmidt, M., Vereecken, H., Western, A., Hendricks Franssen, H.-J., 2021. Improving the representation of cropland sites in the community land model (CLM) version 5.0. Geosci. Model Dev. 14, 573–601. https://doi.org/10.5194/gmd-14-573-2021.

Bonan, G.B., Patton, E.G., Finnigan, J.J., Baldocchi, D.D., Harman, I.N., 2021. Moving beyond the incorrect but useful paradigm: reevaluating big-leaf and multilayer plant canopies to model biosphere-atmosphere fluxes – a review. Agric. For. Meteorol. 306, 108435 https://doi.org/10.1016/j.agrformet.2021.108435.

Breusch, T.S., Pagan, A.R., 1979. A simple test for heteroscedasticity and random coefficient variation. Econometrica 47, 1287. https://doi.org/10.2307/1911963.

Broddrick, J.T., Ware, M.A., Jallet, D., Palsson, B.O., Peers, G., 2022. Integration of physiologically relevant photosynthetic energy flows into whole genome models of light-driven metabolism. Plant J. 112, 603–621. https://doi.org/10.1111/tpj.15965.

Burnham, K.P., Anderson, D.R., Burnham, K.P., 2002. Model Selection and Multimodel Inference: A Practical Information-Theoretic Approach, 2nd ed. Springer, New York.

Camino, C., Gonzalez-Dugo, V., Hernandez, P., Zarco-Tejada, P.J., 2019. Radiative transfer Vcmax estimation from hyperspectral imagery and SIF retrievals to assess photosynthetic performance in rainfed and irrigated plant phenotyping trials. Remote Sensing of Environment 231, 111186. https://doi.org/10.1016/j.rse.2019.05.005.

Cano, F.J., Sánchez-Gómez, D., Rodríguez-Calcerrada, J., Warren, C.R., Gil, L., Aranda, I., 2013. Effects of drought on mesophyll conductance and photosynthetic limitations at different tree canopy layers: limitations to carbon uptake into the canopy. Plant Cell Environ. https://doi.org/10.1111/pce.12103.

Cendrero-Mateo, M.P., Carmo-Silva, A.E., Porcar-Castell, A., Hamerlynck, E.P., Papuga, S.A., Moran, M.S., 2015. Dynamic response of plant chlorophyll fluorescence to light, water and nutrient availability. Funct. Plant Biol. 42, 746. https://doi.org/10.1071/FP15002.

Cendrero-Mateo, Wieneke, Damm, Alonso, Pinto, Moreno, Guanter, Celesti, Rossini, Sabater, Cogliati, Julitta, Rascher, Goulas, Aasen, Pacheco-Labrador, Arthur, 2019. Sun-induced chlorophyll fluorescence III: benchmarking retrieval methods and sensor characteristics for proximal sensing. Remote Sens. 11, 962. https://doi.org/10.3390/rs11080962.

Chang, C.Y., Guanter, L., Frankenberg, C., Köhler, P., Gu, L., Magney, T.S., Grossmann, K., Sun, Y., 2020. Systematic assessment of retrieval methods for canopy far-red solar-induced chlorophyll fluorescence using high-frequency automated Field spectroscopy. J. Geophys. Res. Biogeosci. 125 https://doi.org/10.1029/2019JG005533 e2019JG005533.

Chang, C.Y., Wen, J., Han, J., Kira, O., LeVonne, J., Melkonian, J., Riha, S.J., Skovira, J., Ng, S., Gu, L., Wood, J.D., Näthe, P., Sun, Y., 2021. Unpacking the drivers of diurnal dynamics of sun-induced chlorophyll fluorescence (SIF): canopy structure, plant physiology, instrument configuration and retrieval methods. Remote Sens. Environ. 265, 112672 https://doi.org/10.1016/j.rse.2021.112672.

Chang, T.-G., Shi, Z., Zhao, H., Song, Q., He, Z., Van Rie, J., Den Boer, B., Galle, A., Zhu, X.-G., 2022. 3dCAP-Wheat: An Open-Source Comprehensive Computational Framework Precisely Quantifies Wheat Foliar, Nonfoliar, and Canopy Photosynthesis. Plant Phenomics 2022, 2022/9758148. https://doi.org/10.34133/2022/9758148.

Chen, J., Liu, X., Du, S., Ma, Y., Liu, L., 2020. Integrating SIF and clearness index to improve maize GPP estimation using continuous tower-based observations. Sensors 20, 2493. https://doi.org/10.3390/s20092493.

Chen, R., Liu, L., Liu, X., Liu, Z., Gu, L., Rascher, U., 2024. Improving estimates of sub-daily gross primary production from solar-induced chlorophyll fluorescence by accounting for light distribution within canopy. Remote Sensing of Environment 300, 113919. https://doi.org/10.1016/j.rse.2023.113919.

Chen, X., Mo, X., Hu, S., Liu, S., 2019. Relationship between fluorescence yield and photochemical yield under water stress and intermediate light conditions. J. Exp. Bot. 70, 301–313. https://doi.org/10.1093/jxb/ery341.

Chu, H., Baldocchi, D.D., John, R., Wolf, S., Reichstein, M., 2017. Fluxes all of THE time? A primer on THE temporal representativeness of fluxnet: Fluxes all of the time? J. Geophys. Res. Biogeosci. 122, 289–307. https://doi.org/10.1002/2016JG003576.

Chu, H., Luo, X., Ouyang, Z., Chan, W.S., Dengel, S., Biraud, S.C., Torn, M.S., Metzger, S., Kumar, J., Arain, M.A., Arkebauer, T.J., Baldocchi, D., Bernacchi, C., Billesbach, D., Black, T.A., Blanken, P.D., Bohrer, G., Bracho, R., Brown, S., Brunsell, N.A., Chen, J., Chen, X., Clark, K., Desai, A.R., Duman, T., Durden, D., Fares, S., Forbrich, I., Gamon, J.A., Gough, C.M., Griffis, T., Helbig, M., Hollinger, D., Humphreys, E., Ikawa, H., Iwata, H., Ju, Y., Knowles, J.F., Knox, S.H., Kobayashi, H., Kolb, T., Law, B., Lee, X., Litvak, M., Liu, H., Munger, J.W., Noormets, A., Novick, K., Oberbauer, S.F., Oechel, W., Oikawa, P., Papuga, S.A., Pendall, E., Prajapati, P., Prueger, J., Quinton, W.L., Richardson, A.D., Russell, E.S., Scott, R.L., Starr, G., Staebler, R., Stoy, P.C., Stuart-Haëntjens, E., Sonnentag, O., Sullivan, R.C., Suyker, A., Ueyama, M., Vargas, R., Wood, J.D., Zona, D., 2021. Representativeness of Eddy-covariance flux footprints for areas surrounding AmeriFlux sites. Agric. For. Meteorol. 301–302, 108350 https://doi.org/10.1016/j.agrformet.2021.108350.

Coble, A.P., Fogel, M.L., Parker, G.G., 2017. Canopy gradients in leaf functional traits for species that differ in growth strategies and shade tolerance. Tree Physiol. 37, 1415–1425. https://doi.org/10.1093/treephys/tpx048.

Cowan, I., Farquhar, G., 1977. Stomatal function in relation to leaf metabolism and environment. Symp. Soc. Exp. Biol. 31, 471–505.

Crous, K.Y., Uddling, J., De Kauwe, M.G., 2022. Temperature responses of photosynthesis and respiration in evergreen trees from boreal to tropical latitudes. New Phytol. 234, 353–374. https://doi.org/10.1111/nph.17951.

Damm, A., Elbers, J., Erler, A., Gioli, B., Hamdi, K., Hutjes, R., Kosvancova, M., Meroni, M., Miglietta, F., Moersch, A., Moreno, J., Schickling, A., Sonnenschein, R., Udelhoven, T., Van Der Linden, S., Hostert, P., Rascher, U., 2010. Remote sensing of sun-induced fluorescence to improve modeling of diurnal courses of gross primary production (GPP). Glob. Chang. Biol. 16, 171–186. https://doi.org/10.1111/j.1365-2486.2009.01908.x.

De Cannière, S., Herbst, M., Vereecken, H., Defourny, P., Jonard, F., 2021. Constraining water limitation of photosynthesis in a crop growth model with sun-induced chlorophyll fluorescence. Remote Sens. Environ. 267, 112722 https://doi.org/10.1016/j.rse.2021.112722.

De Cannière, S., Vereecken, H., Defourny, P., Jonard, F., 2022. Remote sensing of instantaneous drought stress at canopy level using Sun-induced chlorophyll fluorescence and canopy reflectance. Remote Sens. 14, 2642. https://doi.org/10.3390/rs14112642.

Dechant, B., Ryu, Y., Badgley, G., Köhler, P., Rascher, U., Migliavacca, M., Zhang, Y., Tagliabue, G., Guan, K., Rossini, M., Goulas, Y., Zeng, Y., Frankenberg, C., Berry, J. A., 2022. NIRVP: A robust structural proxy for sun-induced chlorophyll fluorescence and photosynthesis across scales. Remote Sensing of Environment 268, 112763. https://doi.org/10.1016/j.rse.2021.112763.

Dechant, B., Ryu, Y., Badgley, G., Zeng, Y., Berry, J.A., Zhang, Y., Goulas, Y., Li, Z., Zhang, Q., Kang, M., Li, J., Moya, I., 2020. Canopy structure explains the relationship between photosynthesis and sun-induced chlorophyll fluorescence in crops. Remote Sens. Environ. 241, 111733 https://doi.org/10.1016/j.rse.2020.111733.

Demmig-Adams, B., Adams III, W.W., 2006. Photoprotection in an ecological context: the remarkable complexity of thermal energy dissipation. New Phytologist 172, 11–21. https://doi.org/10.1111/j.1469-8137.2006.01835.x.

Drusch, M., Moreno, J., Del Bello, U., Franco, R., Goulas, Y., Huth, A., Kraft, S., Middleton, E.M., Miglietta, F., Mohammed, G., Nedbal, L., Rascher, U., Schuttemeyer, D., Verhoef, W., 2017. The FLuorescence EXplorer Mission concept—ESA's earth Explorer 8. IEEE Trans. Geosci. Remote Sens. 55, 1273–1284. https://doi.org/10.1109/TGRS.2016.2621820.

Dumont, B., Heinesch, B., Bodson, B., Bogaerts, G., Chopin, H., De Ligne, A., Demoulin, L., Douxfils, B., Engelmann, T., Faurès, A., Longdoz, B., Manise, T., Orgun, A., Piret, A., Thyrion, T., 2023. ETC L2 ARCHIVE, Lonzee, 2016-12-31–2023-09-30.

Erenstein, O., Jaleta, M., Mottaleb, K.A., Sonder, K., Donovan, J., Braun, H.-J., 2022. Global trends in wheat production, consumption and trade. In: Reynolds, M.P., Braun, H.-J. (Eds.), Wheat Improvement. Springer International Publishing, Cham, pp. 47–66. https://doi.org/10.1007/978-3-030-90673-3_4.

Farquhar, G.D., von Caemmerer, S., Berry, J.A., 1980. A biochemical model of photosynthetic CO2 assimilation in leaves of C3 species. Planta 149, 78–90. https://doi.org/10.1007/BF00386231.

Feng, H., Xu, T., Liu, L., Zhou, S., Zhao, J., Liu, S., Xu, Z., Mao, K., He, X., Zhu, Z., Chai, L., 2021. Modeling transpiration with Sun-induced chlorophyll fluorescence observations via carbon-water coupling methods. Remote Sens. 13, 804. https://doi.org/10.3390/rs13040804.

Flexas, J., Escalona, J.M., Evain, S., Gulías, J., Moya, I., Osmond, C.B., Medrano, H., 2002. Steady-state chlorophyll fluorescence (Fs) measurements as a tool to follow variations of net CO2 assimilation and stomatal conductance during water-stress in C3 plants. Physiologia Plantarum 114, 231–240. https://doi.org/10.1034/j.1399-3054.2002.1140209.x.

Franck, F., Juneau, P., Popovic, R., 2002. Resolution of the photosystem I and photosystem II contributions to chlorophyll fluorescence of intact leaves at room temperature. Biochim. Biophys. Acta BBA - Bioenerg. 1556, 239–246. https://doi.org/10.1016/S0005-2728(02)00366-3.

Friedlingstein, P., O'Sullivan, M., Jones, M.W., Andrew, R.M., Gregor, L., Hauck, J., Le Quéré, C., Luijkx, I.T., Olsen, A., Peters, G.P., Peters, W., Pongratz, J., Schwingshackl, C., Sitch, S., Canadell, J.G., Ciais, P., Jackson, R.B., Alin, S.R., Alkama, R., Arneth, A., Arora, V.K., Bates, N.R., Becker, M., Bellouin, N., Bittig, H.C., Bopp, L., Chevallier, F., Chini, L.P., Cronin, M., Evans, W., Falk, S., Feely, R.A., Gasser, T., Gehlen, M., Gkritzalis, T., Gloege, L., Grassi, G., Gruber, N., Gürses, Ö., Harris, I., Hefner, M., Houghton, R.A., Hurtt, G.C., Iida, Y., Ilyina, T., Jain, A.K., Jersild, A., Kadono, K., Kato, E., Kennedy, D., Klein Goldewijk, K., Knauer, J., Korsbakken, J.I., Landschützer, P., Lefèvre, N., Lindsay, K., Liu, J., Liu, Z., Marland, G., Mayot, N., McGrath, M.J., Metzl, N., Monacci, N.M., Munro, D.R., Nakaoka, S.-I., Niwa, Y., O'Brien, K., Ono, T., Palmer, P.I., Pan, N., Pierrot, D., Pocock, K., Poulter, B., Resplandy, L., Robertson, E., Rödenbeck, C., Rodriguez, C., Rosan, T.M., Schwinger, J., Séférian, R., Shutler, J.D., Skjelvan, I., Steinhoff, T., Sun, Q., Sutton, A.J., Sweeney, C., Takao, S., Tanhua, T., Tans, P.P., Tian, X., Tian, H., Tilbrook, B., Tsujino, H., Tubiello, F., Van Der Werf, G.R., Walker, A.P., Wanninkhof, R., Whitehead, C., Willstrand Wranne, A., Wright, R., Yuan, W., Yue, C., Yue, X., Zaehle, S., Zeng, J., Zheng, B., 2022. Global carbon budget 2022. Earth Syst. Sci. Data 14, 4811–4900. https://doi.org/10.5194/essd-14-4811-2022.

Furbank, R.T., Quick, W.P., Sirault, X.R.R., 2015. Improving photosynthesis and yield potential in cereal crops by targeted genetic manipulation: Prospects, progress and challenges. Field Crops Research 182, 19–29. https://doi.org/10.1016/j.fcr.2015.04.009.

Genty, B., Wonders, J., Baker, N.R., 1990. Non-photochemical quenching of Fo in leaves is emission wavelength dependent: consequences for quenching analysis and its interpretation. Photosynth. Res. 26, 133–139. https://doi.org/10.1007/BF00047085.

Gourlez de la Motte, L., Beauclaire, Q., Heinesch, B., Cuntz, M., Foltýnová, L., Sigut, L., Kowalska, N., Manca, G., Ballarin, I., Vincke, C., Roland, M., Ibrom, A., Lousteau, D., Siebicke, L., Bernard, L., 2020. Non-stomatal processes reduce gross primary productivity in temperate forest ecosystems during severe edaphic drought. Philos. Trans. R. Soc. B Biol. Sci. https://doi.org/10.1098/RSTB-2019-0527. In Press.

Granier, A., Bréda, N., Biron, P., Villette, S., 1999. A lumped water balance model to evaluate duration and intensity of drought constraints in forest stands. Ecol. Model. 116, 269–283. https://doi.org/10.1016/S0304-3800(98)00205-1.

Gu, L., Han, J., Wood, J.D., Chang, C.Y., Sun, Y., 2019. Sun-induced Chl fluorescence and its importance for biophysical modeling of photosynthesis based on light reactions. New Phytol. 223, 1179–1191. https://doi.org/10.1111/nph.15796.

Han, J., Chang, C.Y., Gu, L., Zhang, Y., Meeker, E.W., Magney, T.S., Walker, A.P., Wen, J., Kira, O., McNaull, S., Sun, Y., 2022a. The physiological basis for estimating photosynthesis from Chl *a* fluorescence. New Phytol. 234, 1206–1219. https://doi.org/10.1111/nph.18045.

Han, J., Gu, L., Warren, J.M., Guha, A., Mclennan, D.A., Zhang, W., Zhang, Y., 2022b. The roles of photochemical and non-photochemical quenching in regulating photosynthesis depend on the phases of fluctuating light conditions. Tree Physiol. 42, 848–861. https://doi.org/10.1093/treephys/tpab133.

He, L., Wood, J.D., Sun, Y., Magney, T., Dutta, D., Köhler, P., Zhang, Y., Yin, Y., Frankenberg, C., 2020. Tracking Seasonal and Interannual Variability in Photosynthetic Downregulation in Response to Water Stress at a Temperate Deciduous Forest. JGR Biogeosciences 125, e2018JG005002. https://doi.org/10.1029/2018JG005002.

Hedges, L.V., Gurevitch, J., Curtis, P.S., 1999. The META-analysis of response ratios in experimental ECOLOGY. Ecology 80, 1150–1156. https://doi.org/10.1890/0012-9658(1999)080[1150:TMAORR]2.0.CO;2.

Helm, L.T., Shi, H., Lerdau, M.T., Yang, X., 2020. Solar-induced chlorophyll fluorescence and short-term photosynthetic response to drought. Ecol. Appl. 30 https://doi.org/10.1002/eap.2101.

Huang, G., Yang, Y., Zhu, L., Peng, S., Li, Y., 2021. Temperature responses of photosynthesis and stomatal conductance in rice and wheat plants. Agric. For. Meteorol. 300, 108322 https://doi.org/10.1016/j.agrformet.2021.108322.

Hulley, G.C., Ghent, D., Göttsche, F.M., Guillevic, P.C., Mildrexler, D.J., Coll, C., 2019. 3 - land surface temperature. In: Hulley, G.C., Ghent, D. (Eds.), Taking the Temperature of the Earth. Elsevier, pp. 57–127. https://doi.org/10.1016/B978-0-12-814458-9.00003-4.

Jia, Q., Liu, Z., Guo, C., Wang, Y., Yang, J., Yu, Q., Wang, J., Zheng, F., Lu, X., 2023. Relationship between photosynthetic CO2 assimilation and chlorophyll fluorescence for winter wheat under water stress. Plants 12, 3365. https://doi.org/10.3390/plants12193365.

Jonard, F., De Cannière, S., Brüggemann, N., Gentine, P., Short Gianotti, D.J., Lobet, G., Miralles, D.G., Montzka, C., Pagán, B.R., Rascher, U., Vereecken, H., 2020. Value of sun-induced chlorophyll fluorescence for quantifying hydrological states and fluxes: current status and challenges. Agric. For. Meteorol. 291, 108088 https://doi.org/10.1016/j.agrformet.2020.108088.

Jonard, F., Feldman, A.F., Short Gianotti, D.J., Entekhabi, D., 2022. Observed water and light limitation across global ecosystems. Biogeosciences 19, 5575–5590. https://doi.org/10.5194/bg-19-5575-2022.

Jung, M., Schwalm, C., Migliavacca, M., Walther, S., Camps-Valls, G., Koirala, S., Anthoni, P., Besnard, S., Bodesheim, P., Carvalhais, N., Chevallier, F., Gans, F., Goll, D.S., Haverd, V., Köhler, P., Ichii, K., Jain, A.K., Liu, J., Lombardozzi, D., Nabel, J.E.M.S., Nelson, J.A., O'Sullivan, M., Pallandt, M., Papale, D., Peters, W., Pongratz, J., Rödenbeck, C., Sitch, S., Tramontana, G., Walker, A., Weber, U., Reichstein, M., 2020. Scaling carbon fluxes from eddy covariance sites to globe: synthesis and evaluation of the FLUXCOM approach. Biogeosciences 17, 1343–1365. https://doi.org/10.5194/bg-17-1343-2020.

Kattenborn, T., Richter, R., Guimarães-Steinicke, C., Feilhauer, H., Wirth, C., 2022. AngleCam: predicting the temporal variation of leaf angle distributions from image series with deep learning. Methods Ecol. Evol. 13, 2531–2545. https://doi.org/10.1111/2041-210X.13968.

Keenan, T.F., Migliavacca, M., Papale, D., Baldocchi, D., Reichstein, M., Torn, M., Wutzler, T., 2019. Widespread inhibition of daytime ecosystem respiration. Nat. Ecol. Evol. 3, 407–415. https://doi.org/10.1038/s41559-019-0809-2.

Kim, J., Ryu, Y., Dechant, B., Lee, H., Kim, H.S., Kornfeld, A., Berry, J.A., 2021. Solar-induced chlorophyll fluorescence is non-linearly related to canopy photosynthesis in a temperate evergreen needleleaf forest during the fall transition. Remote Sensing of Environment 258, 112362. https://doi.org/10.1016/j.rse.2021.112362.

Kira, O., Chang, Y.-Y., Gu, L., Wen, J., Hong, Z., Sun, Y., 2021. Partitioning net ecosystem exchange (NEE) of CO2 using solar-induced chlorophyll fluorescence (SIF). Geophys. Res. Lett. 48, e2020GL091247 https://doi.org/10.1029/2020GL091247.

Knauer, J., El-Madany, T.S., Zaehle, S., Migliavacca, M., 2018. Bigleaf—an R package for the calculation of physical and physiological ecosystem properties from eddy covariance data. PLoS One 13, e0201114. https://doi.org/10.1371/journal.pone.0201114.

Koffi, E.N., Rayner, P.J., Norton, A.J., Frankenberg, C., Scholze, M., 2015. Investigating the usefulness of satellite-derived fluorescence data in inferring gross primary productivity within the carbon cycle data assimilation system. Biogeosciences 12, 4067–4084. https://doi.org/10.5194/bg-12-4067-2015.

Kong, J., Ryu, Y., Liu, J., Dechant, B., Rey-Sanchez, C., Shortt, R., Szutu, D., Verfaillie, J., Houborg, R., Baldocchi, D.D., 2022. Matching high resolution satellite data and flux tower footprints improves their agreement in photosynthesis estimates. Agric. For. Meteorol. 316, 108878 https://doi.org/10.1016/j.agrformet.2022.108878.

Kramer, D.M., Johnson, G., Kiirats, O., Edwards, G.E., 2004. New fluorescence parameters for the determination of Q_A redox state and excitation energy fluxes. Photosynth. Res. 79, 209–218. https://doi.org/10.1023/B:PRES.0000015391.99477.0d.

Lasslop, G., Migliavacca, M., Bohrer, G., Reichstein, M., Bahn, M., Ibrom, A., Jacobs, C., Kolari, P., Papale, D., Vesala, T., Wohlfahrt, G., Cescatti, A., 2012. On the choice of the driving temperature for eddy-covariance carbon dioxide flux partitioning. Biogeosciences 9, 5243–5259. https://doi.org/10.5194/bg-9-5243-2012.

Lee, J.-E., Berry, J.A., van der Tol, C., Yang, X., Guanter, L., Damm, A., Baker, I., Frankenberg, C., 2015. Simulations of chlorophyll fluorescence incorporated into the community land model version 4. Glob. Chang. Biol. 21, 3469–3477. https://doi.org/10.1111/gcb.12948.

Li, H., Zhao, C., Yang, G., Feng, H., 2015. Variations in crop variables within wheat canopies and responses of canopy spectral characteristics and derived vegetation indices to different vertical leaf layers and spikes. Remote Sens. Environ. 169, 358–374. https://doi.org/10.1016/j.rse.2015.08.021.

Li, X., Xiao, J., He, B., Altaf Arain, M., Beringer, J., Desai, A.R., Emmel, C., Hollinger, D. Y., Krasnova, A., Mammarella, I., Noe, S.M., Ortiz, P.S., Rey-Sanchez, A.C., Rocha, A. V., Varlagin, A., 2018. Solar-induced chlorophyll fluorescence is strongly correlated with terrestrial photosynthesis for a wide variety of biomes: first global analysis based on OCO-2 and flux tower observations. Glob. Chang. Biol. 24, 3990–4008. https://doi.org/10.1111/gcb.14297.

Li, Q., Gao, Y., Hamani, A.K.M., Fu, Y., Liu, J., Wang, H., Wang, X., 2023. Effects of Warming and Drought Stress on the Coupling of Photosynthesis and Transpiration in Winter Wheat (Triticum aestivum L.). Applied Sciences 13, 2759. https://doi.org/10.3390/app13052759.

Li, Z.-L., Tang, B.-H., Wu, H., Ren, H., Yan, G., Wan, Z., Trigo, I.F., Sobrino, J.A., 2013. Satellite-derived land surface temperature: current status and perspectives. Remote Sens. Environ. 131, 14–37. https://doi.org/10.1016/j.rse.2012.12.008.

Liu, Y., Chen, J.M., He, L., Zhang, Z., Wang, R., Rogers, C., Fan, W., De Oliveira, G., Xie, X., 2022a. Non-linearity between gross primary productivity and far-red solar-induced chlorophyll fluorescence emitted from canopies of major biomes. Remote Sens. Environ. 271, 112896 https://doi.org/10.1016/j.rse.2022.112896.

Liu, Z., Zhao, F., Liu, X., Yu, Q., Wang, Y., Peng, X., Cai, H., Lu, X., 2022b. Direct estimation of photosynthetic CO2 assimilation from solar-induced chlorophyll fluorescence (SIF). Remote Sens. Environ. 271, 112893 https://doi.org/10.1016/j.rse.2022.112893.

Lu, X., Liu, Z., Zhao, F., Tang, J., 2020. Comparison of total emitted solar-induced chlorophyll fluorescence (SIF) and top-of-canopy (TOC) SIF in estimating photosynthesis. Remote Sens. Environ. 251, 112083 https://doi.org/10.1016/j.rse.2020.112083.

Lu, Y., Williams, I.N., Bagley, J.E., Torn, M.S., Kueppers, L.M., 2017. Representing winter wheat in the community land model (version 4.5). Geosci. Model Dev. 10, 1873–1888. https://doi.org/10.5194/gmd-10-1873-2017.

Maes, W.H., Gentine, P., Verhoest, N.E.C., Miralles, D.G., 2019. Potential evaporation at eddy-covariance sites across the globe. Hydrol. Earth Syst. Sci. 23, 925–948. https://doi.org/10.5194/hess-23-925-2019.

Maguire, A.J., Eitel, J.U.H., Griffin, K.L., Magney, T.S., Long, R.A., Vierling, L.A., Schmiege, S.C., Jennewein, J.S., Weygint, W.A., Boelman, N.T., Bruner, S.G., 2020. On the functional relationship between fluorescence and photochemical yields in complex Evergreen Needleleaf canopies. Geophys. Res. Lett. 47 https://doi.org/10.1029/2020GL087858.

Marchin, R.M., Backes, D., Ossola, A., Leishman, M.R., Tjoelker, M.G., Ellsworth, D.S., 2022. Extreme heat increases stomatal conductance and drought-induced mortality risk in vulnerable plant species. Glob. Chang. Biol. 28, 1133–1146. https://doi.org/10.1111/gcb.15976.

Marrs, J.K., Reblin, J.S., Logan, B.A., Allen, D.W., Reinmann, A.B., Bombard, D.M., Tabachnik, D., Hutyra, L.R., 2020. Solar-induced fluorescence does not track photosynthetic carbon assimilation following induced stomatal closure. Geophys. Res. Lett. 47 https://doi.org/10.1029/2020GL087956.

Martini, D., Sakowska, K., Wohlfahrt, G., Pacheco-Labrador, J., van der Tol, C., Porcar-Castell, A., Magney, T.S., Carrara, A., Colombo, R., El-Madany, T.S., Gonzalez-Cascon, R., Martín, M.P., Julitta, T., Moreno, G., Rascher, U., Reichstein, M., Rossini, M., Migliavacca, M., 2022. Heatwave breaks down the linearity between sun-induced fluorescence and gross primary production. New Phytol. 233, 2415–2428. https://doi.org/10.1111/nph.17920.

Maxwell, K., Johnson, G.N., 2000. Chlorophyll fluorescence—a practical guide. J. Exp. Bot. 51, 659–668. https://doi.org/10.1093/jexbot/51.345.659.

Medlyn, B.E., Duursma, R.A., Eamus, D., Ellsworth, D.S., Prentice, I.C., Barton, C.V.M., Crous, K.Y., De Angelis, P., Freeman, M., Wingate, L., 2011. Reconciling the optimal and empirical approaches to modelling stomatal conductance: reconciling optimal and empirical stomatal models. Glob. Chang. Biol. 17, 2134–2144. https://doi.org/10.1111/j.1365-2486.2010.02375.x.

Medlyn, B.E., De Kauwe, M.G., Lin, Y.-S., Knauer, J., Duursma, R.A., Williams, C.A., Arneth, A., Clement, R., Isaac, P., Limousin, J.-M., Linderson, M.-L., Meir, P., Martin-StPaul, N., Wingate, L., 2017. How do leaf and ecosystem measures of water-use efficiency compare? New Phytol. 216, 758–770. https://doi.org/10.1111/nph.14626.

Miner, G.L., Bauerle, W.L., Baldocchi, D.D., 2017. Estimating the sensitivity of stomatal conductance to photosynthesis: a review. Plant Cell & Environment 40, 1214–1238. https://doi.org/10.1111/pce.12871.

Mohammed, G.H., Colombo, R., Middleton, E.M., Rascher, U., van der Tol, C., Nedbal, L., Goulas, Y., Pérez-Priego, O., Damm, A., Meroni, M., Joiner, J., Cogliati, S., Verhoef, W., Malenovský, Z., Gastellu-Etchegorry, J.-P., Miller, J.R., Guanter, L., Moreno, J., Moya, I., Berry, J.A., Frankenberg, C., Zarco-Tejada, P.J., 2019. Remote sensing of solar-induced chlorophyll fluorescence (SIF) in vegetation: 50 years of progress. Remote Sens. Environ. 231, 111177 https://doi.org/10.1016/j.rse.2019.04.030.

Monteith, J.L., 1965. Evaporation and environment. Symp. Soc. Exp. Biol. 19, 205–234.

Moriondo, M., Maselli, F., Bindi, M., 2007. A simple model of regional wheat yield based on NDVI data. Eur. J. Agron. 26, 266–274. https://doi.org/10.1016/j.eja.2006.10.007.

Myneni, R.B., Williams, D.L., 1994. On the relationship between FAPAR and NDVI. Remote Sens. Environ. 49, 200–211. https://doi.org/10.1016/0034-4257(94)90016-7.

Niinemets, Ü., Sonninen, E., Tobias, M., 2004. Canopy gradients in leaf intercellular CO_2 mole fractions revisited: interactions between leaf irradiance and water stress need consideration. Plant Cell Environ. 27, 569–583. https://doi.org/10.1111/j.1365-3040.2003.01168.x.

Niinemets, Ü., Keenan, T.F., Hallik, L., 2015. A worldwide analysis of within-canopy variations in leaf structural, chemical and physiological traits across plant functional types. New Phytol. 205, 973–993. https://doi.org/10.1111/nph.13096.

Ouzounis, T., Razi Parjikolaei, B., Frettac, X., Rosenqvist, E., Ottosen, C.-O., 2015. Predawn and high intensity application of supplemental blue light decreases the quantum yield of PSII and enhances the amount of phenolic acids, flavonoids, and pigments in *Lactuca sativa*. Front. Plant Sci. 6 https://doi.org/10.3389/fpls.2015.00019.

Pastorello, G., Trotta, C., Canfora, E., Chu, H., Christianson, D., Cheah, Y.-W., Poindexter, C., Chen, J., Elbashandy, A., Humphrey, M., Isaac, P., Polidori, D., Ribeca, A., Ingen, C., Zhang, L., Amiro, B., Ammann, C., Arain, M., Ardö, J., Papale, D., 2020. The FLUXNET2015 dataset and the ONEFlux processing pipeline for eddy covariance data. Sci. Data 7. https://doi.org/10.1038/s41597-020-0534-3.

Pfündel, E.E., 2021. Simultaneously measuring pulse-amplitude-modulated (PAM) chlorophyll fluorescence of leaves at wavelengths shorter and longer than 700 nm. Photosynth. Res. 147, 345–358. https://doi.org/10.1007/s11120-021-00821-7.

Pfündel, E.E., Klughammer, C., Meister, A., Cerovic, Z.G., 2013. Deriving fluorometer-specific values of relative PSI fluorescence intensity from quenching of F(0) fluorescence in leaves of *Arabidopsis thaliana* and *Zea mays*. Photosynth. Res. 114, 189–206. https://doi.org/10.1007/s11120-012-9788-8.

Porcar-Castell, A., Tyystjärvi, E., Atherton, J., van der Tol, C., Flexas, J., Pfündel, E.E., Moreno, J., Frankenberg, C., Berry, J.A., 2014. Linking chlorophyll a fluorescence to photosynthesis for remote sensing applications: mechanisms and challenges. J. Exp. Bot. 65, 4065–4095. https://doi.org/10.1093/jxb/eru191.

Porcar-Castell, A., Malenovský, Z., Magney, T., Van Wittenberghe, S., Fernández-Marín, B., Maignan, F., Zhang, Y., Maseyk, K., Atherton, J., Albert, L.P., Robson, T. M., Zhao, F., Garcia-Plazaola, J.-I., Ensminger, I., Rajewicz, P.A., Grebe, S., Tikkanen, M., Kellner, J.R., Ihalainen, J.A., Rascher, U., Logan, B., 2021. Chlorophyll a fluorescence illuminates a path connecting plant molecular biology to earth-system science. Nat. Plants 7, 998–1009. https://doi.org/10.1038/s41477-021-00980-4.

Pradhan, A., Aher, L., Hegde, V., Jangid, K.K., Rane, J., 2022. Cooler canopy leverages sorghum adaptation to drought and heat stress. Sci. Rep. 12, 4603. https://doi.org/10.1038/s41598-022-08590-6.

Rebmann, C., Aubinet, M., Schmid, H., Arriga, N., Aurela, M., Burba, G., Clement, R., De Ligne, A., Fratini, G., Gielen, B., Grace, J., Graf, A., Gross, P., Haapanala, S., Herbst, M., Hörtnagl, L., Ibrom, A., Joly, L., Kljun, N., Kolle, O., Kowalski, A., Lindroth, A., Loustau, D., Mammarella, I., Mauder, M., Merbold, L., Metzger, S., Mölder, M., Montagnani, L., Papale, D., Pavelka, M., Peichl, M., Roland, M., Serrano-Ortiz, P., Siebicke, L., Steinbrecher, R., Tuovinen, J.-P., Vesala, T., Wohlfahrt, G., Franz, D., 2018. ICOS eddy covariance flux-station site setup: a review. Int. Agrophys. 32, 471–494. https://doi.org/10.1515/intag-2017-0044.

Reichstein, M., Falge, E., Baldocchi, D., Papale, D., Aubinet, M., Berbigier, P., Bernhofer, C., Buchmann, N., Gilmanov, T., Granier, A., Grunwald, T., Havrankova, K., Ilvesniemi, H., Janous, D., Knohl, A., Laurila, T., Lohila, A., Loustau, D., Matteucci, G., Meyers, T., Miglietta, F., Ourcival, J.-M., Pumpanen, J., Rambal, S., Rotenberg, E., Sanz, M., Tenhunen, J., Seufert, G., Vaccari, F., Vesala, T., Yakir, D., Valentini, R., 2005. On the separation of net ecosystem exchange into

assimilation and ecosystem respiration: review and improved algorithm. Glob. Chang. Biol. 11, 1424–1439. https://doi.org/10.1111/j.1365-2486.2005.001002.x.
Reichstein, M., Bahn, M., Ciais, P., Frank, D., Mahecha, M.D., Seneviratne, S.I., Zscheischler, J., Beer, C., Buchmann, N., Frank, D.C., Papale, D., Rammig, A., Smith, P., Thonicke, K., van der Velde, M., Vicca, S., Walz, A., Wattenbach, M., 2013. Climate extremes and the carbon cycle. Nature 500, 287–295. https://doi.org/10.1038/nature12350.
Reitz, O., Bogena, H., Neuwirth, B., Sanchez-Azofeifa, A., Graf, A., Bates, J., Leuchner, M., 2023. Environmental drivers of Gross primary productivity and light use efficiency of a temperate spruce forest. J. Geophys. Res. Biogeosci. 128, e2022JG007197 https://doi.org/10.1029/2022JG007197.
Riedesel, L., Möller, M., Horney, P., Golla, B., Piepho, H.-P., Kautz, T., Feike, T., 2023. Timing and intensity of heat and drought stress determine wheat yield losses in Germany. PLoS ONE 18, e0288202. https://doi.org/10.1371/journal.pone.0288202.
Rogers, A., Medlyn, B.E., Dukes, J.S., Bonan, G., von Caemmerer, S., Dietze, M.C., Kattge, J., Leakey, A.D.B., Mercado, L.M., Niinemets, Ü., Prentice, I.C., Serbin, S.P., Sitch, S., Way, D.A., Zaehle, S., 2017. A roadmap for improving the representation of photosynthesis in earth system models. New Phytol. 213, 22–42. https://doi.org/10.1111/nph.14283.
Ryu, Y., Berry, J.A., Baldocchi, D.D., 2019. What is global photosynthesis? History, uncertainties and opportunities. Remote Sens. Environ. 223, 95–114. https://doi.org/10.1016/j.rse.2019.01.016.
Schuttemeyer, D., Burba, M., Drusch, M., Elfving, A., Mecklenburg, S., 2018. ESA's Campaign Activities in Support of the FLEX Mission. In: IGARSS 2018–2018 IEEE International Geoscience and Remote Sensing Symposium. Presented at the IGARSS 2018–2018 IEEE International Geoscience and Remote Sensing Symposium. IEEE, Valencia, pp. 3924–3926. https://doi.org/10.1109/IGARSS.2018.8518034.
Sha, Z., Bai, Y., Li, R., Lan, H., Zhang, X., Li, J., Liu, X., Chang, S., Xie, Y., 2022. The global carbon sink potential of terrestrial vegetation can be increased substantially by optimal land management. Commun. Earth Environ. 3, 8. https://doi.org/10.1038/s43247-021-00333-1.
Shen, Q., Lin, J., Yang, J., Zhao, W., Wu, J., 2022. Exploring the Potential of Spatially Downscaled Solar-Induced Chlorophyll Fluorescence to Monitor Drought Effects on Gross Primary Production in Winter Wheat. IEEE J. Sel. Top. Appl. Earth Observations Remote Sensing 15, 2012–2022. https://doi.org/10.1109/JSTARS.2022.3148393.
Shi, S., Cong, W., Lu, S., Zhao, T., Wang, F., Lu, Q., 2022. Can SIF and NPQ be used in the photosynthesis rate simulation of plants subjected to drought? Environ. Exp. Bot. 203, 105067 https://doi.org/10.1016/j.envexpbot.2022.105067.
Shin, Y.K., Bhandari, S.R., Jo, J.S., Song, J.W., Lee, J.G., 2021. Effect of drought stress on chlorophyll fluorescence parameters, phytochemical contents, and antioxidant activities in lettuce seedlings. Horticulturae 7, 238. https://doi.org/10.3390/horticulturae7080238.
Soudani, K., Hmimina, G., Delpierre, N., Pontailler, J.-Y., Aubinet, M., Bonal, D., Caquet, B., De Grandcourt, A., Burban, B., Flechard, C., Guyon, D., Granier, A., Gross, P., Heinesh, B., Longdoz, B., Loustau, D., Moureaux, C., Ourcival, J.-M., Rambal, S., Saint André, L., Dufrêne, E., 2012. Ground-based Network of NDVI measurements for tracking temporal dynamics of canopy structure and vegetation phenology in different biomes. Remote Sensing of Environment 123, 234–245. https://doi.org/10.1016/j.rse.2012.03.012.
Stocker, B.D., Zscheischler, J., Keenan, T.F., Prentice, I.C., Peñuelas, J., Seneviratne, S.I., 2018. Quantifying soil moisture impacts on light use efficiency across biomes. New Phytol. 218, 1430–1449. https://doi.org/10.1111/nph.15123.
Tarvainen, L., Wallin, G., Räntfors, M., Uddling, J., 2013. Weak vertical canopy gradients of photosynthetic capacities and stomatal responses in a fertile Norway spruce stand. Oecologia 173, 1179–1189. https://doi.org/10.1007/s00442-013-2703-y.
Thom, A.S., 1972. Momentum, mass and heat exchange of vegetation. Q. J. R. Meteorol. Soc. 98, 124–134. https://doi.org/10.1002/qj.49709841510.
van der Tol, C., Verhoef, W., Rosema, A., 2009. A model for chlorophyll fluorescence and photosynthesis at leaf scale. Agric. For. Meteorol. 149, 96–105. https://doi.org/10.1016/j.agrformet.2008.07.007.
van der Tol, C., Berry, J.A., Campbell, P.K.E., Rascher, U., 2014. Models of fluorescence and photosynthesis for interpreting measurements of solar-induced chlorophyll fluorescence. J. Geophys. Res. Biogeosci. 119, 2312–2327. https://doi.org/10.1002/2014JG002713.
Tramontana, G., Migliavacca, M., Jung, M., Reichstein, M., Keenan, T.F., Camps-Valls, G., Ogee, J., Verrelst, J., Papale, D., 2020. Partitioning net carbon dioxide fluxes into photosynthesis and respiration using neural networks. Glob. Chang. Biol. 26, 5235–5253. https://doi.org/10.1111/gcb.15203.
Urban, O., Hlaváčová, M., Klem, K., Novotná, K., Rapantová, B., Smutná, P., Horáková, V., Hlavinka, P., Škarpa, P., Trnka, M., 2018. Combined effects of drought and high temperature on photosynthetic characteristics in four winter wheat genotypes. Field Crop Res. 223, 137–149. https://doi.org/10.1016/j.fcr.2018.02.029.
Van Wittenberghe, S., Adriaenssens, S., Staelens, J., Verheyen, K., Samson, R., 2012. Variability of stomatal conductance, leaf anatomy, and seasonal leaf wettability of young and adult European beech leaves along a vertical canopy gradient. Trees 26, 1427–1438. https://doi.org/10.1007/s00468-012-0714-7.
Verma, M., Schimel, D., Evans, B., Frankenberg, C., Beringer, J., Drewry, D.T., Magney, T., Marang, I., Hutley, L., Moore, C., Eldering, A., 2017. Effect of environmental conditions on the relationship between solar-induced fluorescence and gross primary productivity at an OzFlux grassland site. Journal of Geophysical Research: Biogeosciences 122, 716–733. https://doi.org/10.1002/2016JG003580.
Walker, A.P., Johnson, A.L., Rogers, A., Anderson, J., Bridges, R.A., Fisher, R.A., Lu, D., Ricciuto, D.M., Serbin, S.P., Ye, M., 2021. Multi-hypothesis comparison of Farquhar and Collatz photosynthesis models reveals the unexpected influence of empirical assumptions at leaf and global scales. Glob. Chang. Biol. 27, 804–822. https://doi.org/10.1111/gcb.15366.
Wang, N., Clevers, J.G.P.W., Wieneke, S., Bartholomeus, H., Kooistra, L., 2022. Potential of UAV-based sun-induced chlorophyll fluorescence to detect water stress in sugar beet. Agric. For. Meteorol. 323, 109033 https://doi.org/10.1016/j.agrformet.2022.109033.
Wang, H., Xiao, J., 2021. Improving the Capability of the SCOPE Model for Simulating Solar-Induced Fluorescence and Gross Primary Production Using Data from OCO-2 and Flux Towers. Remote Sensing 13, 794. https://doi.org/10.3390/rs13040794.
Warren, C., 2006. Temperature response of photosynthesis and internal conductance to CO2: results from two independent approaches. J. Exp. Bot. 57, 3057–3067. https://doi.org/10.1093/jxb/erl067.
Williams, I.N., Torn, M.S., Riley, W.J., Wehner, M.F., 2014. Impacts of climate extremes on gross primary production under global warming. Environ. Res. Lett. 9, 094011 https://doi.org/10.1088/1748-9326/9/9/094011.
Wohlfahrt, G., Galvagno, M., 2017. Revisiting the choice of the driving temperature for eddy covariance CO2 flux partitioning. Agric. For. Meteorol. 237–238, 135–142. https://doi.org/10.1016/j.agrformet.2017.02.012.
Wohlfahrt, G., Gerdel, K., Migliavacca, M., Rotenberg, E., Tatarinov, F., Müller, J., Hammerle, A., Julitta, T., Spielmann, F.M., Yakir, D., 2018. Sun-induced fluorescence and gross primary productivity during a heat wave. Sci. Rep. 8, 14169. https://doi.org/10.1038/s41598-018-32602-z.
Xiao, J., Li, X., He, B., Arain, M.A., Beringer, J., Desai, A.R., Emmel, C., Hollinger, D.Y., Krasnova, A., Mammarella, I., Noe, S.M., Serrano Ortiz, P., Rey-Sanchez, C., Rocha, A.V., Varlagin, A., 2019. Solar-induced chlorophyll fluorescence exhibits a universal relationship with gross primary productivity across a wide variety of biomes. Glob. Chang. Biol. 25, e4–e6. https://doi.org/10.1111/gcb.14565.
Xu, S., Atherton, J., Riikonen, A., Zhang, C., Oivukkamäki, J., MacArthur, A., Honkavaara, E., Hakala, T., Koivumäki, N., Liu, Z., Porcar-Castell, A., 2021. Structural and photosynthetic dynamics mediate the response of SIF to water stress in a potato crop. Remote Sens. Environ. 263, 112555 https://doi.org/10.1016/j.rse.2021.112555.
Yang, M., He, J., Sun, Z., Li, Q., Cai, J., Zhou, Q., Wollenweber, B., Jiang, D., Wang, X., 2023. Drought priming mechanisms in wheat elucidated by in-situ determination of dynamic stomatal behavior. Front. Plant Sci. 14, 1138494. https://doi.org/10.3389/fpls.2023.1138494.
Yang, P., van der Tol, C., Verhoef, W., Damm, A., Schickling, A., Kraska, T., Muller, O., Rascher, U., 2019. Using reflectance to explain vegetation biochemical and structural effects on sun-induced chlorophyll fluorescence. Remote Sens. Environ. 231, 110996 https://doi.org/10.1016/j.rse.2018.11.039.
Yang, X., Tang, J., Mustard, J.F., Lee, J.-E., Rossini, M., Joiner, J., Munger, J.W., Kornfeld, A., Richardson, A.D., 2015. Solar-induced chlorophyll fluorescence that correlates with canopy photosynthesis on diurnal and seasonal scales in a temperate deciduous forest. Geophysical Research Letters 42, 2977–2987. https://doi.org/10.1002/2015GL063201.
Yang, P., van der Tol, C., Campbell, P.K.E., Middleton, E.M., 2021. Unraveling the physical and physiological basis for the solar- induced chlorophyll fluorescence and photosynthesis relationship using continuous leaf and canopy measurements of a corn crop. Biogeosciences 18, 441–465. https://doi.org/10.5194/bg-18-441-2021.
Yao, L., Liu, Y., Yang, D., Cai, Z., Wang, J., Lin, C., Lu, N., Lyu, D., Tian, L., Wang, M., Yin, Z., Zheng, Y., Wang, S., 2022. Retrieval of solar-induced chlorophyll fluorescence (SIF) from satellite measurements: comparison of SIF between TanSat and OCO-2. Atmos. Meas. Tech. 15, 2125–2137. https://doi.org/10.5194/amt-15-2125-2022.
Zeng, Y., Badgley, G., Dechant, B., Ryu, Y., Chen, M., Berry, J.A., 2019. A practical approach for estimating the escape ratio of near-infrared solar-induced chlorophyll fluorescence. Remote Sens. Environ. 232, 111209 https://doi.org/10.1016/j.rse.2019.05.028.
Zhang, Y., Guanter, L., Berry, J.A., Joiner, J., Van Der Tol, C., Huete, A., Gitelson, A., Voigt, M., Köhler, P., 2014. Estimation of vegetation photosynthetic capacity from space-based measurements of chlorophyll fluorescence for terrestrial biosphere models. Global Change Biology 20, 3727–3742. https://doi.org/10.1111/gcb.12664.
Zhang, Y., Guanter, L., Berry, J.A., Van Der Tol, C., Yang, X., Tang, J., Zhang, F., 2016. Model-based analysis of the relationship between sun-induced chlorophyll fluorescence and gross primary production for remote sensing applications. Remote Sensing of Environment 187, 145–155. https://doi.org/10.1016/j.rse.2016.10.016.
Zhang, Y., Guanter, L., Joiner, J., Song, L., Guan, K., 2018. Spatially-explicit monitoring of crop photosynthetic capacity through the use of space-based chlorophyll fluorescence data. Remote Sensing of Environment 210, 362–374. https://doi.org/10.1016/j.rse.2018.03.031.
Zhao, F., Guo, Y., Verhoef, W., Gu, X., Liu, L., Yang, G., 2014. A method to reconstruct the solar-induced canopy fluorescence Spectrum from hyperspectral measurements. Remote Sens. 6, 10171–10192. https://doi.org/10.3390/rs61010171.
Zhou, S., Duursma, R.A., Medlyn, B.E., Kelly, J.W.G., Prentice, I.C., 2013. How should we model plant responses to drought? An analysis of stomatal and non-stomatal responses to water stress. Agricultural and Forest Meteorology 182–183, 204–214. https://doi.org/10.1016/j.agrformet.2013.05.009.

Zhou, S.-X., Prentice, I.C., Medlyn, B.E., 2019. Bridging drought experiment and modeling: representing the differential sensitivities of Leaf gas exchange to drought. Front. Plant Sci. 9 https://doi.org/10.3389/fpls.2018.01965.

Zivcak, M., Brestic, M., Kalaji, H.M., Govindjee, 2014. Photosynthetic responses of sun- and shade-grown barley leaves to high light: is the lower PSII connectivity in shade leaves associated with protection against excess of light? Photosynth. Res. 119, 339–354. https://doi.org/10.1007/s11120-014-9969-8.

Zou, X., Mõttus, M., Tammeorg, P., Torres, C.L., Takala, T., Pisek, J., Mäkelä, P., Stoddard, F.L., Pellikka, P., 2014. Photographic measurement of leaf angles in field crops. Agric. For. Meteorol. 184, 137–146. https://doi.org/10.1016/j.agrformet.2013.09.010.